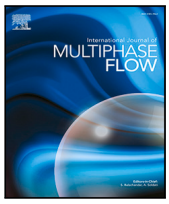
International Journal of Multiphase Flow 198 (2026) 105657



Contents lists available at ScienceDirect

International Journal of Multiphase Flow

journal homepage: www.elsevier.com/locate/ijmulflow



Research Paper

Ellipsoidal particle transport and deposition in an averaged human nasal airway — A CFD study

Jana Wedel [a,*], Nicolás Catalán [b], Paul Steinmann [a,c], Matjaž Hriberšek [d], Salvatore Cito [b], Sylvana Varela [b], Jordi Pallarès [b], Jure Ravnik [d]

[a] Institute of Applied Mechanics, Universität Erlangen-Nürnberg, Germany
[b] Departament d'Enginyeria Mecànica, Universitat Rovira i Virgili, Tarragona, Spain
[c] Glasgow Computational Engineering Center, University of Glasgow, United Kingdom
[d] Faculty of Mechanical Engineering, University of Maribor, Slovenia

ARTICLE INFO

Keywords:
Fibers
CFD
Point–particle
OpenFOAM

ABSTRACT

Airborne particles represent one of the major health challenges of our time, with micron-sized non-spherical particles, particularly fibrous ones, being of particular concern due to their ability to penetrate deep into the lungs and potentially cause disease. Despite their relevance, quantitative studies on the transport and deposition of non-spherical particles in realistic human nasal cavities remain sparse. Anatomical variability further complicates this problem, yet the limited availability of nasal cavity geometries restricts systematic investigation. To address this, we employ an averaged nasal cavity geometry, derived from multiple realistic replicas, to assess the influence of breathing scenarios on non-spherical particle transport and deposition.

Fluid and particle simulations were conducted using an in-house OpenFOAM (V11) module in an Euler–Lagrangian framework, with steady RANS-based flow fields resolved using the k–ω SST turbulence model. Breathing conditions corresponding to rest and moderate exercise (7.5, 15, and 30 L/min) were studied for particles with d_{eq} = 2.5–20 µm, considering both spherical and prolate ellipsoidal particles of different aspect ratios.

Our results demonstrate that flow rate as well as both particle size and shape strongly influence deposition efficiency and local deposition patterns. Higher flow rates strongly amplify deposition hotspots while altering their distribution. Importantly, we show that simplified shape-factor models systematically overpredict deposition efficiencies for strongly elongated particles and misrepresent local deposition patterns compared to the Euler–Lagrange Euler-Rotation (EL-ER) approach. Note that mispredicted spatial deposition could lead to underestimating particle exposure to sensitive lung regions, misjudging drug delivery efficiency, or overlooking health risks from fibrous or elongated particles, highlighting the importance of an accurate representation of non-spherical, i.e. ellipsoidal, particle dynamics.

1. Introduction

1.1. Exposure to hazardous particles

Humans inhale more than 100 million airborne particles each day, including mold spores, silica dust, volcanic ash, asbestos fibers, exhaust residues, and pollen, many of which pose serious health risks (Li et al., 2007; Kleinstreuer and Feng, 2013). Public health concerns related to inhaled particles have long been recognized, with well-documented examples such as cigarette smoke and asbestos exposure. The COVID-19 pandemic further intensified research on aerosols and droplets (Balachandar and Soldati, 2020; Balachandar et al., 2020; Wang et al., 2021; Wedel et al., 2021b, 2022). While aerosols are commonly modeled as spherical due to dominant surface tension effects at small scales, real-world particles such as asbestos, silica dust, and pollen exhibit a wide variety of non-spherical shapes. Their orientation strongly influences their motion and deposition, making their behavior more complex than that of simple spheres (Ravnik et al., 2022). This complexity is particularly relevant for asbestos, which remains the leading cause of occupational mortality worldwide, with more than 200,000 deaths annually and over 125 million people at risk (World Health Organization; International Labour Organization, 2021; Gualtieri, 2023). Microplastics represent another growing concern. Detected in multiple human organs (including the respiratory tract, digestive system, and even the brain), they enter the body through ingestion, dermal contact,

* Corresponding author.
E-mail address: jana.wedel@fau.de (J. Wedel).

https://doi.org/10.1016/j.ijmultiphaseflow.2026.105657
Received 15 September 2025; Received in revised form 9 January 2026; Accepted 9 February 2026
Available online 10 February 2026
0301-9322/© 2026 The Authors. Published by Elsevier Ltd. This is an open access article under the CC BY license (http://creativecommons.org/licenses/by/4.0/).

and inhalation (Nihart et al., 2025; Zarus et al., 2021; Yang et al., 2023). Daily inhalation has been estimated at 26–130 airborne particles (Prata, 2018), with some studies reporting values exceeding 270 particles during light activity (Vianello et al., 2019). Indoor exposure is particularly high due to fibers released from textiles, carpets, and upholstery. Microplastic inhalation has been linked to inflammation, carcinogenesis, and the worsening of chronic conditions such as asthma and COPD (Liu et al., 2024; Paplińska-Goryca et al., 2025). Their diverse geometries, ranging from spheres to irregular fragments and fibers, further complicate the prediction of their deposition and health impact (Zhang et al., 2024, 2020).

1.2. The human nasal passages

The nasal cavity plays a central role in both protecting the lungs and enabling intranasal drug delivery. Its narrow and sinuous passages warm and humidify incoming air while filtering particulates, shielding the alveoli but leaving the epithelium vulnerable to repeated exposure. At the same time, this filtering capability has been harnessed in spray-based delivery systems for locally and systemically acting drugs, with applications in neurodegenerative diseases and brain tumors (Singh et al., 2001; Inthavong et al., 2008; Shen et al., 2025). The nasal cavity's large surface area and vascularization allow for rapid absorption, and direct nose-to-brain pathways enable drugs to bypass the blood–brain barrier. Thus, quantifying particle deposition in the nasal passages is critical for both health risk assessment and therapeutic optimization.

Experimental studies consistently show that deposition efficiency increases with particle size in the inertial regime (1–10 μm), ranging from nearly 0% at 1 μm to nearly complete deposition at 10 μm (Schroeter et al., 2011). However, both in vivo studies and nasal replica experiments face limitations. Human studies capture realistic physiology but are constrained by variability and narrow test ranges. Replica casts expand experimental conditions but introduce surface imperfections that can alter airflow and deposition (Kelly et al., 2004a; Schroeter et al., 2011). For instance, Kelly et al. (2004a) observed differences in deposition between casts produced with different stereolithography techniques, highlighting the sensitivity of deposition to even small variations in surface detail.

Computational fluid dynamics (CFD) offers a complementary approach by simulating airflow and particle transport in anatomically realistic models reconstructed from medical imaging (Prinz et al., 2025; Wedel et al., 2022; Schroeter et al., 2011). Most studies focus primarily on the temporal evolution of airflow fields during respiration. For instance, Dong et al. (2022) investigated airflow patterns across three life stages, specifically infant, young adult, and elderly, and highlighted the significance of anatomical differences. Their results showed that variations in nasal cavity size and shape significantly impact the velocity field, emphasizing the need to consider the subject's age in such studies.

Various strategies have been employed to investigate particle deposition within the nasal cavity, with particle size identified as a critical factor. For spherical particles, Wang et al. (2009) studied the effect of particle size on deposition and found that particles larger than 1 μm tended to deposit near the nostrils, while nanoparticles distributed more uniformly throughout the cavity. Similarly, Zamankhan et al. (2006) observed that particles smaller than 20 nm deposited primarily via diffusion. Interestingly, while Wang et al. (2009) reported a direct relationship between flow rate and deposition, Zamankhan et al. concluded that flow rate had no significant effect on nanoparticle deposition.

Schroeter et al. (2011) investigated how geometric variations between CFD models and physical nasal replicas affect particle deposition. Using CFD models generated from the same MRI data as the nasal replica described in Kelly et al. (2004a), the authors examined models with varying degrees of surface smoothness. Through simulations of steady-state inspiratory airflow and Lagrangian particle tracking, they found that smoother CFD models consistently under-predicted nasal deposition compared to the physical replica, aligning with earlier findings. To address these discrepancies, the authors incorporated surface artifacts (features absent in the smoothed models) and plotted deposition efficiency against the Stokes number, using a characteristic diameter derived from the pressure drop across the nasal cavity. This adjustment accounted for differences in airflow resistance caused by wall roughness. The study reinforces the importance of even minor geometric details in accurately predicting nasal particle deposition and emphasizes the need to consider these factors when comparing CFD results with experimental data from nasal replica casts.

In addition, particle shape has been recognized as playing a critical role in particle deposition. In the case of non-spherical or fiber-like particles, such as asbestos, many studies account for non-sphericity by employing shape factors, see for example (Hu et al., 2023; Jia et al., 2018; Inthavong et al., 2008, 2021; Riaz et al., 2025). Dastan et al. (2014) compared this approach with the drag model proposed by Haider and Levenspiel (Haider and Levenspiel, 1989), concluding that the latter overestimated fiber deposition in specific regions of the nasal cavity. A similar approach was taken by Hu et al. (2023), who analyzed the deposition of pollen in pediatric nasal cavities by assuming prolate ellipsoidal particles. Their findings showed that most particles were deposited in the nasopharynx, suggesting a potential link between adenoid hypertrophy and particle retention.

A key limitation in many of these studies is the assumption of steady, laminar flow, which overlooks the time-dependent nature of breathing and the effects of turbulence. Time evolution of airflow is crucial, as shown in Hu et al. (2023), where turbulent effects were considered and shown to influence particle deposition patterns. As highlighted by Gorlé et al. (2009), both velocity and turbulent kinetic energy significantly affect particle trajectories, making it essential to ensure mesh-independent simulations for both flow quantities to achieve reliable and physically accurate results. Nevertheless, most studies only provide mesh independence analysis focusing on the fluid velocity, Dastan et al. (2014), Schroeter et al. (2011), Inthavong et al. (2021). For further details on flow and particle transport and deposition in the human respiratory tract using CFD various excellent review papers have been published, see for example (Rahim et al., 2020; Bui et al., 2020; Kleinstreuer and Feng, 2013; Rostami, 2009; Lancmanová and Bodnar, 2025).

As highlighted, inhaled particles represent a persistent health challenge, with the nasal cavity serving both as the body's first line of defense and as a promising site for therapeutic delivery. Accurate prediction of deposition requires accounting for particle properties, airflow conditions, anatomical complexity, and turbulence, combining insights from experiments and computational models.

Despite the extensive body of work on nasal particle transport and deposition, most computational studies of non-spherical particles rely on simplified representations, such as equivalent spheres or empirical shape factors, and neglect particle orientational dynamics altogether. While such approaches can capture first-order effects of non-sphericity, they cannot resolve orientation-dependent forces, torques, and wall-contact behavior that govern the transport and deposition of elongated or anisotropic particles. In this context, the present study applies an orientation-resolving Euler–Lagrange Euler-Rotation (EL-ER) framework for non-spherical particle tracking to a human nasal cavity replica. Building on our previously developed and validated particle model (Wedel et al., 2023), the aim of this work is to systematically investigate shape- and orientation-dependent particle transport and deposition in the nasal passages and to quantify differences relative to commonly used shape-factor-based modeling approaches.

Note that resolving particle orientation has direct implications for applications where elongated or anisotropic particles dominate inhalation exposure or therapeutic delivery. For fibrous particles such as asbestos or microplastic fibers, orientation determines local aerodynamic response, wall-interaction geometry, and contact mechanics, which in

turn influence deposition hot spots and residence times in sensitive regions of the nasal cavity. Similarly, emerging intranasal drug delivery concepts increasingly employ non-spherical or fiber-like carriers to enhance adhesion, targeting, or transport efficiency, Shachar-Berman et al. (2020). In these contexts, models relying on equivalent-sphere assumptions or empirical shape factors may lead to biased deposition predictions and misrepresentation of regional exposure. By enabling orientation-resolved transport and deposition modeling, the present framework provides a quantitative basis for assessing the validity of simplified approaches and for improving predictive capability in health risk assessment and therapeutic design.

1.3. Outline of the study

The paper is organized as follows: In Section 2, the governing equations for carrier flow and ellipsoidal particles are presented. Furthermore, in Section 3, the numerical setup is introduced including the airway geometry considered, the particle properties as well as the model validation. Next, in Section 4, the steady-state inhalation flow field approach together with Lagrangian particle tracking is applied to the averaged human nasal geometry to investigate the particle transport and deposition at steady state inhalation. Finally, Section 5 summarizes the work presented and highlights the main conclusions.

2. Governing equations

In the following, the dynamics of dilute particle suspensions in fluid flows are detailed.

2.1. Carrier flow

Among the various modeling approaches, the Reynolds-Averaged Navier–Stokes (RANS) method remains the most widely used for simulating pulmonary airflow, primarily due to its relatively low computational cost, albeit at the expense of reduced accuracy (Bui et al., 2020). For instance, Zhang and Kleinstreuer (Zhang and Kleinstreuer, 2011) studied airflow in the upper human airway and observed that RANS, when coupled with the standard k-ω turbulence model, generally failed to achieve the accuracy of Large Eddy Simulation (LES) (Bui et al., 2020). Nevertheless, they also found that employing RANS with the k-ω SST model in simplified lung geometries containing only a few bifurcations produced results that aligned well with LES predictions.

In this study, we solve the flow field in the nasal airway using an Eulerian framework. Following the approach of Wedel et al. (2021b,a, 2022), we employ the open-source CFD software OpenFOAM (V11) (OpenFOAM The OpenFOAM Foundation, 2025; Weller et al., 1998) to compute the steady-state incompressible flow in an averaged nasal geometry. The governing steady-state incompressible RANS equations are expressed as follows (Weller et al., 1998)

$$\boldsymbol{\nabla}\cdot\left[\rho_{\mathrm{f}}\bar{\boldsymbol{u}}\otimes\bar{\boldsymbol{u}}+\boldsymbol{\tau}^{\mathrm{RANS}}\right]=-\boldsymbol{\nabla}\bar{p}+\boldsymbol{\nabla}\cdot\bar{\boldsymbol{\tau}}+\bar{\boldsymbol{f}}_{\mathrm{D}} \tag{1}$$

and

$$\mathrm{div}\bar{\boldsymbol{u}}=0\,. \tag{2}$$

Moreover, the Reynolds stress $\boldsymbol{\tau}^{\mathrm{RANS}}$ and the mean viscous stress $\bar{\boldsymbol{\tau}}$ expand as (Ferziger and Perić, 2008)

$$\boldsymbol{\tau}^{\mathrm{RANS}}:=\rho_{\mathrm{f}}\overline{\boldsymbol{u}_i'\otimes\boldsymbol{u}_j'}\qquad\text{and}\qquad\bar{\boldsymbol{\tau}}:=\mu\,\boldsymbol{\nabla}^{\mathrm{SYM}}\bar{\boldsymbol{u}}\,. \tag{3}$$

OpenFOAM employs the finite volume method (FVM) to discretize the governing equations. In Eqs. (1)–(3), $\bar{\boldsymbol{u}}$, $\bar{p}$, and ρ_{f} represent the Reynolds-averaged fluid velocity, pressure, and fluid density, respectively. The prime symbol ($'$) in Eq. (3) denotes fluctuations, such that the total velocity field is given by $\boldsymbol{u}=\bar{\boldsymbol{u}}+\boldsymbol{u}'$. While $\bar{\boldsymbol{f}}_{\mathrm{D}}$ generally accounts for body forces acting on the flow, in the present configuration no such forces are considered, and thus $\bar{\boldsymbol{f}}_{\mathrm{D}}=\boldsymbol{0}$.

To close the RANS equations, a turbulence model must be introduced to define the Reynolds stress term $\boldsymbol{\tau}^{\mathrm{RANS}}$. In this study, the k–$\omega$ SST model is used (Ferziger and Perić, 2008; Strelets, 2001).

2.2. Particle equations of motion

In CFD, particle transport is typically modeled using either a Lagrangian or Eulerian framework (Bui et al., 2020). The Lagrangian approach is generally suitable for particles with diameters $d_{\mathrm{eq}}>0.3\,\mu\mathrm{m}$, whereas the Eulerian approach is considered more appropriate for smaller particles with $d_{\mathrm{eq}}<0.3\,\mu\mathrm{m}$ (Bui et al., 2020). Comprehensive reviews of both modeling strategies are provided by Rostami (2009) and Tang and Guo (Tang and Guo, 2011). In this study, we examine particle sizes in the range of $2.5\ \mu\mathrm{m}\le d_{\mathrm{eq}}\le 20\ \mu\mathrm{m}$, i.e. $d_{\mathrm{eq}}>0.3\,\mu\mathrm{m}$, and thus adopt the Lagrangian framework to describe the motion of the dispersed phase (Greifzu et al., 2016). The particles are modeled as point particles (rigid), and thus, no discretization of the particle is required.

2.2.1. Dynamics of translational motion

In general, the trajectory of a particle is determined by its interaction with the surrounding fluid flow. In this work, particle transport is described in an Euler–Lagrangian framework. The particles are tracked using the Maxey–Riley–Gatignol equation, (Maxey and Riley, 1983; Gatignol, 1983), which was proposed to model the motion of small rigid particles. Furthermore, we employ the Brenner drag expression, (Brenner, 1963), to model the drag for arbitrarily shaped particles. Taken together, the employed particle barycentric dynamics read as (Maxey and Riley, 1983; Brenner, 1963; Gatignol, 1983)

$$m_{\mathrm{p}}\frac{d\boldsymbol{v}}{dt}=\boldsymbol{g}V_{\mathrm{p}}\left[\rho_{\mathrm{p}}-\rho_{\mathrm{f}}\right]+\pi\rho_{\mathrm{f}}\nu_{\mathrm{f}}a_3\boldsymbol{K}\cdot[\boldsymbol{u}-\boldsymbol{v}]\,, \tag{4}$$

where gravity, buoyancy, and hydrodynamic drag are taken into account. Contributions from pressure-gradient, added-mass, history, aerodynamic lift, and higher-order effects are neglected (Cui et al., 2018). This modeling choice is justified for the present case of micron-sized particles characterized by a low Stokes number ($\mathrm{Stk}\ll 1$) and a particle density exceeding the fluid density ($\rho_{\mathrm{p}}>\rho_{\mathrm{f}}$). In this regime, particle dynamics are dominated by drag and gravity/buoyancy, while additional contributions remain small. A detailed discussion of this approximation is provided in our previous work (Wedel et al., 2023), and a brief summary is given in Appendix A.

In Eq. (4) $\boldsymbol{v}$, m_{p}, V_{p}, a_3, ρ_{p}, denote the particle velocity, mass, volume, semi-minor particle axis, and density, respectively. The particle volume V_{p} is computed using $V_{\mathrm{p}}=d_{\mathrm{eq}}^3\pi/6$, with d_{eq} labeling the volume equivalent spherical diameter. Furthermore, $\boldsymbol{u}$, ρ_{f}, and ν_{f} label the fluid velocity, fluid density, and kinematic viscosity. In addition, $\boldsymbol{K}$ is the translational resistance tensor. Note that in Eq. (4), $D/Dt=\partial/\partial t+[\boldsymbol{u}\cdot\boldsymbol{\nabla}]$ describes the time derivative following the fluid element, while $d/dt=\partial/\partial t+[\boldsymbol{v}\cdot\boldsymbol{\nabla}]$ represents the time derivative following the Lagrangian particle. The drag force $\boldsymbol{f}_{\mathrm{D}}$ exerted on a superellipsoidal particle moving in a fluid is obtained using (Štrakl et al., 2022)

$$\boldsymbol{f}_{\mathrm{D}}=\int_{\partial\mathcal{B}}\boldsymbol{t}\,\mathrm{d}a=\int_{\partial\mathcal{B}}\boldsymbol{\sigma}\cdot\boldsymbol{n}\,\mathrm{d}a\,\hat{=}\,\pi\rho_{\mathrm{f}}\nu_{\mathrm{f}}a_3\underline{K}\cdot\underline{u}\qquad\text{with}\qquad\underline{K}=\underline{R}^{t}\,\underline{K}'\,\underline{R}\,, \tag{5}$$

where $\boldsymbol{t}=\boldsymbol{\sigma}\cdot\boldsymbol{n}$ denotes the boundary traction. Furthermore, $\underline{K}$ is the translational resistance tensor coefficient matrix in the inertial frame of reference (iFoR). To relate $\underline{K}$ to $\underline{K}'$, the resistance tensor coefficient matrix in the particle frame of reference (pFoR), the rotation matrix $\underline{R}$ is used. Only for limited particle shapes, there exist analytical expressions for $\underline{K}'$. For example, for prolate ellipsoidal particles $\underline{K}'$ reduces to a function of the particle aspect ratio ($\lambda=\lambda_1$) as detailed in Appendix B. These expressions are not available for more general particle shapes. In this case, DNS simulations as employed in Štrakl et al. (2022), can be utilized to determine the translational resistance tensor.

2.2.2. Dynamics of rotational motion

To account for the orientational dynamics of non-spherical particles, we enhance the Euler–Lagrange framework with Euler-Rotations (EL-ER). The rotational motion of an arbitrarily shaped particle moving in a fluid can be described in the pFoR as follows

$$T_1' = J_{11}' \frac{d\,\omega_1'}{dt} - \omega_2'\omega_3' \left[J_{22}' - J_{33}'\right], \tag{6}$$

$$T_2' = J_{22}' \frac{d\,\omega_{22}'}{dt} - \omega_3'\omega_1' \left[J_{33}' - J_{11}'\right], \tag{7}$$

$$T_3' = J_{33}' \frac{d\,\omega_3'}{dt} - \omega_1'\omega_2' \left[J_{11}' - I_{22}'\right], \tag{8}$$

where J_{11}', J_{22}', J_{33}' are the particle moments of inertia about the principal axes (the principal values of the particle's inertia tensor). Moreover, T_1', T_2', T_3' and ω_1', ω_2', ω_3' denote the hydrodynamic torques on the particle and the particle's angular velocities with respect to the principal axes. The moments of inertia for certain particle shapes are detailed in Appendix B.

Taking both rotational and shear flow contributions into account, the torque can be expressed as (Štrakl et al., 2022)

$$\boldsymbol{T} = \int_{\partial\mathcal{B}} \boldsymbol{r} \times \boldsymbol{t}\, \mathrm{d}a \mathrel{\hat{=}} \pi\mu a_3^3 \left[\underline{\Pi}' \cdot \begin{bmatrix} f \\ g \\ h \end{bmatrix} + \underline{\Omega}' \cdot \begin{bmatrix} \xi - \omega_{x'} \\ \eta - \omega_{y'} \\ \chi - \omega_{z'} \end{bmatrix} \right], \tag{9}$$

where $\underline{\Omega}'$ is the rotation resistance coefficient matrix and $\underline{\Pi}'$ the deformation resistance coefficient matrix in the pFoR. In addition, f, g, h denote the off-diagonal elements of the deformation rate tensor and ξ, η and χ are spin tensor components, which are given by

$$f = \frac{1}{2}\left[\frac{\partial u_{z'}}{\partial y} + \frac{\partial u_{y'}}{\partial z}\right], \quad g = \frac{1}{2}\left[\frac{\partial u_{x'}}{\partial z} + \frac{\partial u_{z'}}{\partial x}\right], \quad h = \frac{1}{2}\left[\frac{\partial u_{x'}}{\partial y} + \frac{\partial u_{y'}}{\partial x}\right], \tag{10}$$

$$\xi = \frac{1}{2}\left[\frac{\partial u_{z'}}{\partial y} - \frac{\partial u_{y'}}{\partial z}\right], \quad \eta = \frac{1}{2}\left[\frac{\partial u_{x'}}{\partial z} - \frac{\partial u_{z'}}{\partial x}\right], \quad \chi = \frac{1}{2}\left[\frac{\partial u_{y'}}{\partial x} - \frac{\partial u_{x'}}{\partial y}\right]. \tag{11}$$

The tensor coefficients of $\underline{\Pi}'$ and $\underline{\Omega}'$ can be obtained analytically for only a few particle shapes. For prolate ellipsoidal particles ($\lambda_1 > \lambda_2$, $\lambda_2 = 1$), these are detailed in Appendix B.

For more complex-shaped particles, models such as presented by Štrakl et al. (2022), which rely on dedicated DNS studies, can be employed to model the tensor coefficients of $\underline{\Pi}'$ and $\underline{\Omega}'$.

The orientation of particles in space can be parameterized by Euler angles $[\phi_1, \phi_2, \phi_3]$. However, this leads to a singularity for $\phi_2 = 0$ and $\phi_2 = \pi$. To overcome this drawback, the orientation in space is described by quaternions $\underline{q} = [q_0, q_1, q_2, q_3]^t$. The Euler parameters (quaternions) can be determined using

$$\underline{q} = \begin{bmatrix} q_0 \\ q_1 \\ q_2 \\ q_3 \end{bmatrix} = \begin{bmatrix} \cos\left[0.5\left[\phi_1 + \phi_3\right]\right]\cos\left[\phi_2/2\right] \\ \cos\left[0.5\left[\phi_1 - \phi_3\right]\right]\sin\left[\phi_2/2\right] \\ \sin\left[0.5\left[\phi_1 - \phi_3\right]\right]\sin\left[\phi_2/2\right] \\ \sin\left[0.5\left[\phi_1 + \phi_3\right]\right]\cos\left[\phi_2/2\right] \end{bmatrix} \tag{12}$$

and are subject to the constraint $q_0^2 + q_1^2 + q_2^2 + q_3^2 = 1$, Goldstein (1980). The rotation matrix in the inertia frame follows as

$$\underline{R} = \begin{bmatrix} q_0^2 + q_1^2 - q_2^2 - q_3^2 & 2[q_1q_2 + q_0q_3] & 2[q_1q_3 - q_0q_2] \\ 2[q_1q_2 - q_0q_3] & q_0^2 - q_1^2 + q_2^2 - q_3^2 & 2[q_2q_3 - q_0q_1] \\ 2[q_1q_3 + q_0q_2] & 2[q_2q_3 - q_0q_1] & q_0^2 - q_1^2 - q_2^2 + q_3^2 \end{bmatrix}. \tag{13}$$

In addition, the evolution of $\underline{q}$ is related to the angular particle velocity $\underline{\omega}'$ in the pFoR as

$$\begin{bmatrix} dq_0/dt \\ dq_1/dt \\ dq_2/dt \\ dq_3/dt \end{bmatrix} = \frac{1}{2}\begin{bmatrix} -q_1 & -q_2 & -q_3 \\ q_0 & -q_3 & q_2 \\ q_3 & q_0 & -q_1 \\ -q_2 & q_1 & q_0 \end{bmatrix} \underline{\omega}'. \tag{14}$$

2.3. Shape factors

To evaluate the present nonspherical particle model based on the EL-ER approach, in which particle orientational dynamics are explicitly resolved, against commonly used shape-factor formulations, the shape-factor concept is briefly introduced in the following, together with the specific shape factors employed for comparison in this study. By default, OpenFOAM evaluates the drag force acting on suspended particles using the following formulation

$$\boldsymbol{f}_\mathrm{D} = \frac{3}{4}\frac{\rho_\mathrm{f}}{\rho_\mathrm{p}}\frac{m_\mathrm{p}}{d_\mathrm{p}} c_\mathrm{D} \boldsymbol{u}_\mathrm{rel} |\boldsymbol{u}_\mathrm{rel}|, \tag{15}$$

where c_D denotes the drag coefficient. For spherical particles (using the *sphereDrag* model in OpenFOAM), the drag coefficient is given by

$$c_\mathrm{D} := \begin{cases} 24\mathrm{Re}_\mathrm{p}^{-1}[1 + \mathrm{Re}_\mathrm{p}^{2/3}/6]; & \mathrm{Re}_\mathrm{p} \le 1000\,. \\ 0.424; & \mathrm{Re}_\mathrm{p} \ge 1000\,. \end{cases} \tag{16}$$

with the particle Reynolds number defined as

$$\mathrm{Re}_\mathrm{p} = \frac{d_\mathrm{eq}|\boldsymbol{u}_\mathrm{rel}|}{\nu_\mathrm{f}}, \tag{17}$$

Here, $\boldsymbol{u}_\mathrm{rel} = \boldsymbol{u} - \boldsymbol{v}$ denotes the relative velocity between the particle $\boldsymbol{v}$ and the fluid $\boldsymbol{u}$. For ellipsoidal and other non-spherical particles, there is not a large variety of standard OpenFOAM drag models, however, due to the open-source nature of the program customized models can be straightforwardly implemented. In the literature, we find that for non-spherical particles the drag coefficient is typically described either as a function of the particle's Reynolds number Re_p alone or in combination with shape factors, Farkas et al. (2019). These shape factors are dimensionless quantities that modify the drag force equations to account for deviations from a spherical shape, Farkas et al. (2019). To date, several types of shape factors have been proposed in the literature. One commonly used way to estimate the shape factors is to employ the particle sphericity (ϕ), which was first introduced by Wadell (1933). Sphericity is defined as the ratio between the surface area of a sphere that has the same volume as the particle A_eq and the actual surface area A of the particle

$$\phi = \frac{A_\mathrm{eq}}{A} = \frac{\pi d_\mathrm{eq}^2}{A}. \tag{18}$$

Several researchers (see for example Ganser, 1993; Haider and Levenspiel, 1989; Hartman et al., 1994) have proposed mathematical expressions for the drag coefficient that apply to different ranges of Re_p and ϕ. Among these, the formulation developed by Haider and Levenspiel (HL) (Haider and Levenspiel, 1989) is commonly used, Farkas and Balásházy (2008), Štrakl et al. (2022), Wedel et al. (2023). According to their approach, the drag coefficient (c_D) expands as

$$c_\mathrm{D} = \frac{24}{\mathrm{Re}_\mathrm{p}}\left[1 + t_1\mathrm{Re}_\mathrm{p}^{t_2}\right] + \frac{t_3\mathrm{Re}_\mathrm{p}}{t_4 + \mathrm{Re}_\mathrm{p}}, \tag{19}$$

with

$$\begin{aligned} t_1 &= \exp\left(2.3288 - 6.4581\phi + 2.4486\phi^2\right) \\ t_2 &= 0.0964 + 0.5565\phi \\ t_3 &= \exp\left(4.905 - 13.8944\phi + 18.4222\phi^2 - 10.2599\phi^3\right) \\ t_4 &= \exp\left(1.4681 + 12.2584\phi - 20.7322\phi^2 + 15.8855\phi^3\right). \end{aligned} \tag{20}$$

Haider and Levenspiel (1989), reported that their empirical equations yield accurate results for isometric particles with shape factors

$\phi > 0.67$. Still, their accuracy decreases significantly for more non-spherical particles, i.e. $\phi < 0.23$. Notably, the non-spherical particles examined in this study have shape factor values of $\phi \geq 0.5883$. Note that this model is included in the standard OpenFOAM implementation, where it is referred to as the *nonSphereDrag* model.

Next to the HL model, the Tran–Cong (TC) (Tran-Cong et al., 2004) model is widely used, see for example in Farkas et al. (2019). The TC model incorporates particle circularity (c) and the ratio of the surface-equivalent diameter d_a to the volume-equivalent diameter d_{eq}, i.e. $r = d_a/d_{eq}$ in determining the drag coefficient. In this approach, circularity c serves as a substitute for ϕ to describe the non-sphericity and expands as

$$c = \frac{\pi d_a}{P_p}, \tag{21}$$

where P_p denotes the projected perimeter of the particle in its direction of motion. Taken together, the drag coefficient (c_D) expands as

$$c_D = \frac{24}{\mathrm{Re}_p}\left[1 + \frac{0.15}{\sqrt{c}}\left[r\mathrm{Re}_p\right]^{0.687}\right] + \frac{0.42r^2}{\sqrt{c}\left[1 + 42500\left[r\mathrm{Re}_p\right]^{-1.16}\right]}. \tag{22}$$

Since the fiber orientation varies over time, the circularity needs to be modified at every time step of the particle tracking.

2.4. Turbulent dispersion model

To account for particle–turbulence interactions within the RANS framework, the instantaneous fluid velocity $\mathbf{u} = \bar{\mathbf{u}} + \mathbf{u}'$ is needed, i.e., the sum of the mean velocity $\bar{\mathbf{u}}$ and the fluctuating component $\mathbf{u}'$. However, since the RANS equations only provide the mean velocity $\bar{\mathbf{u}}$, additional modeling is necessary to approximate the fluctuating component $\mathbf{u}'$. In this study, we utilize the *StochasticDispersionRAS* model available in OpenFOAM (V11) (OpenFOAM The OpenFOAM Foundation, 2025). This model introduces velocity fluctuations $\mathbf{u}'$ in random directions based on a Gaussian distribution with zero mean and variance $\sigma^2 = 2k/3$, Koullapis et al. (2017). The fluctuations are related to the turbulent kinetic energy k as follows

$$\mathbf{u}' = \xi\mathbf{d}\sqrt{\frac{2}{3}k}. \tag{23}$$

Here, $\mathbf{d}$ denotes an additional random unit vector, ξ a random number with zero mean and unit variance of Gaussian distribution, Greifzu et al. (2016). It is important to note that the model assumes isotropic turbulence, which defines the standard deviation σ as

$$\sigma = \sqrt{\frac{2}{3}k} = \sqrt{u_1'^2} = \sqrt{u_2'^2} = \sqrt{u_3'^2}, \tag{24}$$

with the velocity coefficients in Cartesian coordinates denoted by u_1, u_2, u_3, Jundi (2016) and Greifzu et al. (2016).

2.5. Equivalent sphere

Accurately capturing the complex motion of irregularly shaped particles is challenging. As a result, equivalent sphere models are commonly employed to approximate the behavior of non-spherical particles.

2.5.1. Equivalent aerodynamic diameter

One widely adopted model is the equivalent aerodynamic sphere for elongated ellipsoidal particles, proposed by Stöber (1972). In this model, the aerodynamic diameter d_a of an ellipsoid expands as

$$d_a = d_{eq}\sqrt{\frac{\rho_p}{\rho_0 K_r}}, \tag{25}$$

where d_{eq} denotes the volume equivalent sphere diameter, ρ_p the particle density, $\rho_0 = 1000\,\mathrm{kg/m^3}$ the reference density, and K_r the dynamic shape factor. Note that K_r expands for prolate spheroids as a function of the dynamic shape factor for the ellipsoid in two different orientations, $K_\parallel$ (principal axis of the prolate ellipsoid is aligned with the main flow) and $K_\perp$ (principal axis of the prolate ellipsoid is perpendicular to the main flow):

$$\frac{1}{K_r} = \frac{1}{3K_\parallel} + \frac{2}{3K_\perp}, \tag{26}$$

which expand as

$$K_\perp = \frac{8\left[\lambda_1^2 - 1\right]\lambda_1^{-1/3}}{3\left[\left[2\lambda_1^2 - 3\right]\ln\left[\lambda_1 + \sqrt{\lambda_1^2 - 1}\right]/\left[\sqrt{\lambda_1^2 - 1}\right] + \lambda_1\right]} \tag{27}$$

and

$$K_\parallel = \frac{4\left[\lambda_1^2 - 1\right]\lambda_1^{-1/3}}{3\left[\left[2\lambda_1^2 - 1\right]\ln\left[\lambda_1 + \sqrt{\lambda_1^2 - 1}\right]/\left[\sqrt{\lambda_1^2 - 1}\right] - \lambda_1\right]}. \tag{28}$$

2.5.2. Equivalent Stokes diameter

Based on the translational resistance tensor components, Fan and Ahmadi (1995) defined the Stokes diameter for an ellipsoidal fiber as

$$d_{\mathrm{Stk,F}} = 6a_3\frac{2\lambda_1}{k'_{11} + k'_{22} + k'_{33}}. \tag{29}$$

Building on the above expression and incorporating the influence of particle density, Dastan et al. (2014) proposed the equivalent Stokes sphere diameter for an ellipsoidal fiber as

$$d_{\mathrm{Stk,D}} = \sqrt{\frac{\rho_p}{\rho_0}}\,d_{\mathrm{Stk,F}}. \tag{30}$$

2.6. Stokes number and the characteristic diameter of the nose

There is considerable variation in nasal anatomy across individuals (Guilmette et al., 1997; Liu et al., 2009), which contributes to pronounced differences in the nasal deposition of micron-scale particles among people (Garcia et al., 2009). Nevertheless, these anatomical differences can be addressed by analyzing deposition behavior in relation to the Stokes number, defined as

$$\mathrm{Stk} = \frac{d_a U}{18\mu_f D_c} \propto \frac{d_a^2 Q}{c D_c^3} \propto \frac{1}{D_c^3} d_a^2 Q =: \mathrm{Stk}^*, \tag{31}$$

where d_a denotes the aerodynamic particle diameter, U the characteristic fluid velocity and D_c the characteristic diameter of the nasal geometry. Note that U can be expressed as $U = Q/cD_c^2$, where Q denotes the flow rate per nostril and c is a constant, which is commonly ignored ($c = 1$) (Garcia et al., 2009). Aerosol theory (see Hinds, 1999) states that when particle deposition due to inertial effects is plotted against the Stokes number, data from different nasal anatomies should align along a single curve. However, this theoretical prediction has yet to be confirmed experimentally, partly because it is challenging to define a representative characteristic diameter D_c for the complex geometry of the nasal cavity, Schroeter et al. (2011).

Recently, Garcia et al. (2009) proposed that a characteristic diameter of the nasal airways can be derived from pressure-flow relationships. For turbulent flow through a smooth pipe of diameter D and length L, the pressure drop ΔP is given by (White, 2008; Schroeter et al., 2011)

$$\Delta P = RQ^{1.75} \quad \text{and} \quad R = 0.241\frac{L\rho_f^{3/4}\mu_f^{1/4}}{D^{19/4}}, \tag{32}$$

i.e., a rearrangement of the Darcy–Weisbach equation using the Blasius correlation. Recall that Q is the volumetric flow per nostril, ρ_f the fluid velocity, μ_f the fluid dynamic viscosity, while R denotes the flow resistance. Using $L := L_{\mathrm{nose}}$ as the length from the nostrils to the end of the septum and $R := R_{\mathrm{nose}} = \Delta p/Q^{1.75}$, $\rho_f = 1.204\,\mathrm{kg/m^3}$ and

$\mu_f = 1.8 \times 10^{-5}\,\mathrm{kg/[m\,s]}$ Garcia et al. (2009) deduced the characteristic diameter of a nose as

$$D_c = \left[0.0181\, L_{nose}/R_{nose}\right]^{4/19}. \tag{33}$$

Using the above definition for D_c, Garcia et al. (2009) succeeded in collapsing deposition data from four different nasal replicas onto a single curve.

In the majority of nasal deposition studies (Inthavong et al., 2008, 2011; Liu et al., 2007; Shang et al., 2015; Shen et al., 2025; Shi et al., 2007), a single nasal geometry was used, resulting in a constant value for D_c, Garcia et al. (2009). Under these conditions and by recalling the relation between volume equivalent diameter d_{eq} and aerodynamic diameter d_a (see Eq. (25)), the Stokes number can be further simplified and is commonly referred to as the Impaction Parameter (IP) (Garcia et al., 2009):

$$\mathrm{IP} = d_a^2 Q = \left[d_{eq}\sqrt{\frac{\rho_p}{\rho_0\, K_r}}\right]^2 Q. \tag{34}$$

In vitro experiments using nasal replicas from a single person (i.e. a constant D_c) have demonstrated that, when deposition efficiency DE is plotted against the Impaction Parameter IP, data from various airflow rates align along a single curve. This finding supports the idea that the deposition of particles in the $1 - 12\,\mu m$ range is primarily controlled by inertial impaction. Schroeter et al. (2011). CFD studies examining laminar vs turbulent airflow conditions have shown that deposition curves do not always collapse when plotted against IP alone. For instance, particle deposition behavior can differ noticeably between laminar and turbulent regimes, indicating that IP scaling may fail across different flow regimes, Schroeter et al. (2011).

3. Numerical simulation

In this study, CFD coupled with Lagrangian particle tracking is used to simulate the dispersion and deposition of ellipsoidal particles within an average human nasal cavity. A range of inhalation flow rates, representing conditions from rest to intense physical activity, is examined. This section begins with a description of the nasal airway geometry used in the simulations, followed by an overview of the numerical setup and solution parameters implemented in the open-source software.

3.1. Nasal airway models

The human nasal cavity is a complex geometry and consists of a multitude of different regions as displayed in Fig. 1. The nasal cavity geometry extends from the nostrils to the nasopharynx.

The geometry of the nasal airways is highly subject-specific, (Brüning et al., 2020), and can be obstructed due to certain diseases. To avoid subject-specific bias, the present study employs a human nasal airway replica that represents an average of 25 subject-specific nasal geometries, (Brüning et al., 2020). For details on the employed averaging technique, see Brüning et al. (2020). Fig. 1(a) depicts a realistic subject-specific nasal cavity replica, while (b) visualizes the employed averaged nasal cavity. As observed, the averaged geometry does not capture all the anatomical regions represented in the subject-specific model, such as the frontal and ethmoid sinuses, and the maxillary sinuses (chambers connected to the nasal cavity through small orifices). Several numerical studies have examined airflow within these cavities during normal breathing and generally concluded that the velocities in these regions are negligible compared to those in the nasal cavity (Tretiakow et al., 2023, 2022).

3.2. Solution setting

In this section, the solution settings for both fluid phase and particles are detailed.

Table 1
Computational details of the considered lung model.

Flow solver:	RANS with k-ω SST (Menter, 1994)
Inlet BC.:	p: totalPressure[a] / u: pressureInletOutletVelocity[b]
Outlet BC.:	p: zeroGradient / u: specified flow rates

[a] Chosen to avoid backflow at inlet.

[b] Flow out of the domain uses a zero gradient condition, while flow into the domain computes a velocity based on the flux in the patch-normal direction (OpenFOAM The OpenFOAM Foundation, 2025).

3.2.1. Fluid

In the present study, we assume standard conditions for air, i.e., air density $\rho_f = 1.225\,\mathrm{kg/m^3}$ and dynamic viscosity of $\mu_f = 1.7894 \times 10^{-5}\,\mathrm{kg/[m\,s]}$. The airflow is assumed to be incompressible and steady-state. As stated in Section 2.1, we employ RANS with k-ω SST turbulence model.

In this study, we examine the following three different breathing rates Q per nostril, ranging from low to moderate activity level, i.e.

- $Q = 3.75\,\mathrm{L/min}$ ($Q_{total} = 2\,Q = 7.5\,\mathrm{L/min}$): Resting or sedentary state (such as sitting quietly). This is in the typical range of resting minute ventilation for a healthy adult ($Q_{total} = 6 - 8\,\mathrm{L/min}$) (Weinberger et al., 2014).
- $Q = 7.5\,\mathrm{L/min}$ ($Q_{total} = 15\,\mathrm{L/min}$): Light physical activity (e.g., slow walking, driving a car Int Panis et al., 2010).
- $Q = 15\,\mathrm{L/min}$ ($Q_{total} = 30\,\mathrm{L/min}$): Moderate physical activity (e.g., brisk walking, light cycling, climbing stairs), Holmér et al. (2007).

The averaged nasal cavity model of Brüning et al. (2020), employed in this study, is shown in Fig. 1(b). The boundary condition used and solver information for the steady-state approach are provided in Table 1, which mimics that breath originates from the alveoli of the lungs.

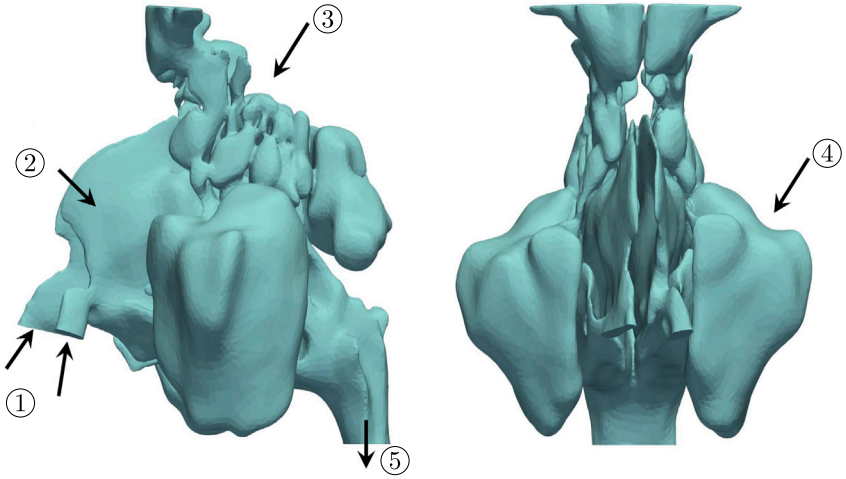
3.2.2. Particles

In the scope of this work, we study rigid particles with a density of $\rho_p = 1830\,\mathrm{kg/m^3}$ to mimic typical microplastics and asbestos fiber particles, which are reported to possess a density range of $1000 \leq \rho_p \leq 2000\,\mathrm{kg/m^3}$, see Tadas et al. (2011), Dang Khoa et al. (2022) and Koelmans et al. (2022). In line with the study of Abolhassantash et al. (2020), 10000 particles were released in each airway passage, i.e., a total of 20000 randomly distributed particles at the entrance of each nasal airway, to ensure statistically robust results.

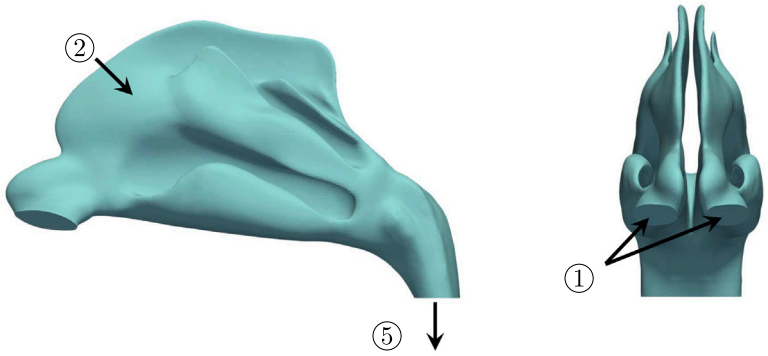
Particles are injected with the local flow velocity, and their initial angular velocity is set to half the local vorticity. To avoid any numerical influence of the inlet boundary condition and to prevent instantaneous fiber deposition at the moment of injection, particles are not released directly on the inlet patches. Instead, for each nostril, particles are injected from a circular region located on an auxiliary injection plane inside the nasal cavity. This injection plane is defined as a plane parallel to the corresponding nostril inlet patch and is obtained by translating the inlet plane by 0.5 mm along its inward-pointing normal direction into the nasal cavity. A circular injection region of diameter 5.6 mm is defined on each injection plane. The center of each circular injection region is obtained by translating the geometric center of the corresponding nostril inlet by the same 0.5 mm displacement, ensuring alignment between the inlet and injection regions.

In agreement with our previous studies (see Wedel et al., 2021b,a, 2022), the airway walls are assumed to be perfectly adhesive, such that particles adhere to the wall upon contact with the internal airway surfaces (Koullapis et al., 2017). Accordingly, particle–wall interactions are modeled using a *touch-stick* deposition mechanism, in which particles deposit upon first contact without rebound or re-entrainment, as detailed in Wedel et al. (2024). A brief summary of the employed collision model is provided in Appendix C.

Particle deposition is evaluated based on the interaction of Lagrangian particles with the wall boundary patches of the computational



(a) Realistic model



(b) Averaged model

Fig. 1. Side and front view of (a) a subject-specific human nasal cavity compared to (b) the averaged human nasal cavity as presented by Brüning et al. (2020). Note that the size ratios of the different geometries are not representative, as they were modified for presentation purposes. (1) nostrils, (2) nasal cavity, (3) frontal and ethmoid sinuses (4) maxillary sinuses, (5) nasopharynx.

domain. Within the OpenFOAM framework, deposition is recorded individually for each wall patch, where a particle is considered deposited once it intersects a depositing boundary and is subsequently removed from the simulation. The total number of deposited particles is obtained by summing the deposition counts over all wall boundary patches. Particles that do not deposit on any boundary during the simulated time interval are assumed to leave the computational domain through outlet boundaries and are therefore not counted as deposited.

Depending on the lung ventilation considered, we adjust the time step to ensure a maximum particle Courant number of $\mathrm{Co_p} \leq 0.3$. Note that $\mathrm{Co_p}$ defines the ratio of the particle displacement within one time step to a characteristic cell length, i.e.,

$$\mathrm{Co_p} = \frac{|\boldsymbol{v}|\,\Delta t}{\Delta x}, \tag{35}$$

where $\boldsymbol{v}$ denotes the particle velocity, Δt the particle time step, and Δx a representative grid spacing.

Table 2 contains a detailed summary of the computational details used for the particle tracking.

3.3. Limitations

The constraints of the current setup align with those identified in our earlier studies (Wedel et al., 2021b,a) and stem from the fundamental characteristics of the Lagrangian point–particle approach and the employed turbulence model:

Table 2
Computational details of particle tracking.

Time integration scheme	Implicit Euler
Forces on particles	Drag[a], gravity/buoyancy (see Eq. (4))
Wall interaction	Touch & Stick[b]
Turbulent dispersion	Continuous random walk
Number of particles	2 × 10000

[a] Analytical drag model for prolate ellipsoids (see Appendix B).
[b] Collision model as presented in Wedel et al. (2024) (see Appendix C).

- **Micro-sized particles**: We assume that the particles are sufficiently small, i.e. smaller than the Kolmogorov length scale η_K, so that the point–particle approach holds.
- **Small particle Reynolds number**: We assume that the particle Reynolds number is sufficiently small so that the local flow around the particle can be described by Stokes flow.
- **Dilute flow**: We consider sufficiently dilute particle suspensions to safely assume a one-way coupling approach, where the fluid is agnostic to the particles and the particles are agnostic to each other.
- **isotropic turbulence**: As we employ the k-ω SST RANS turbulence model we inherit the assumption of isotropic turbulence.

The suitability of the RANS turbulence model with one-way coupling for the flow and particle conditions considered was established

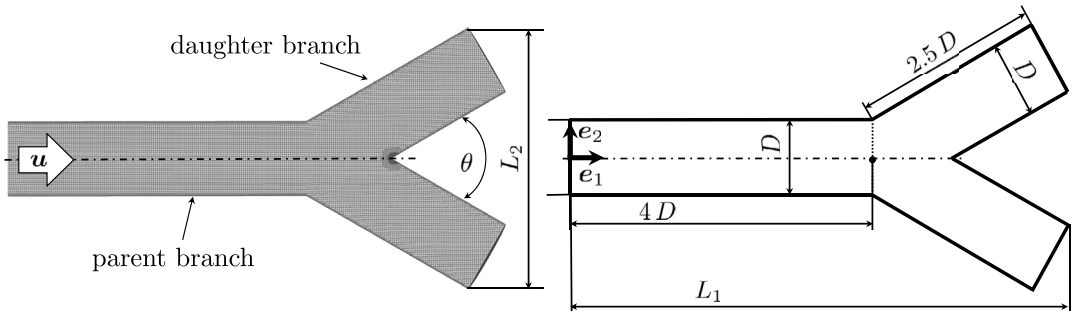


Fig. 2. Simplified bifurcation model (right) and corresponding computational mesh (left). The geometry consists of a parent and daughter airway with diameter $D = 6\,\text{mm}$ and a bifurcation angle of $\theta = 60°$, consistent with Feng and Kleinstreuer (2013). Gravity is oriented along the streamwise $\boldsymbol{e}_1$ direction. The overall model length in $\boldsymbol{e}_1$ is $L_1 = 0.04\,\text{m}$, and the width in $\boldsymbol{e}_2$ is $L_2 = 0.021\,\text{m}$.

in Wedel et al. (2021b,a), and is thus assumed to be equally appropriate for the present study.

3.4. Model validation - Simple bifurcation

To validate the EL-ER approach and assess the accuracy of the considered shape factor models (HL Haider and Levenspiel, 1989 and TC Tran-Cong et al., 2004), we first investigate the transport and deposition of 10^4 ellipsoidal particles in a simplified three-dimensional bifurcating airway model. The geometry and flow parameters follow the configuration of Feng and Kleinstreuer (2013), consisting of a parent and two daughter branches with a diameter of $D = 6\,\text{mm}$, a bifurcation angle of $\theta = 60°$, and a Reynolds number of $\text{Re} = 500$. As noted by Zhang et al. (1996), $\text{Re} = 500$ corresponds to typical breathing conditions in the third generation of the human airway tree. The bifurcation geometry and the computational mesh used in the simulations are shown in Fig. 2.

As shown in Fig. 3(a), the present EL-ER particle approach exhibits excellent agreement in deposition efficiency (DE) for fibrous particles with $\lambda_1 = 20$, closely matching the reference data of Feng and Kleinstreuer (2013). For comparison, results for spherical particles are also included, revealing substantially higher deposition in the same geometry compared to fibrous particles with identical d_{eq}.

Subsequently, we evaluate the EL-ER approach predictions against the simplified shape factor models across different aspect ratios. For $\lambda_1 = 20$, both shape factor models considerably overpredict deposition for $\text{Stk} \geq 0.05$, with the TC model (Tran-Cong et al., 2004) performing slightly better than the HL model (Haider and Levenspiel, 1989). Similar trends are observed for $\lambda_1 = 10$, where overprediction persists but is less pronounced, with deviations reaching up to 10%, again with TC outperforming HL. For $\lambda_1 = 5$, the discrepancies further diminish, though remain notable.

In summary, the EL-ER approach reliably reproduces the reference results, while the shape factor models provide reasonable accuracy only for less elongated particles $\lambda_1 = 5$ and fail to capture the behavior of strongly elongated particles $\lambda_1 \geq 10$.

4. Results

The following section presents the mesh study, as well as the flow rate and particle deposition study.

4.1. Mesh study

To ensure grid-independent results, a mesh convergence study is conducted using four different mesh resolutions. Table 3 summarizes the characteristics of the generated meshes for the airway model.

Table 3
Computational details of generated meshes for the considered nasal cavity.

MeshID	M1	M2	M3	M4
Cells	≈2.9 Mio	≈4 Mio	≈6 Mio	≈8 Mio
Boundary layers	7	7	7	7
Near wall distance	$y^+ \approx 1$	$y^+ \approx 1$	$y^+ \approx 1$	$y^+ \approx 1$

These are then used to compare the velocity and turbulent kinetic energy distributions as part of the grid independence assessment. As an example, the overall geometry and mesh resolution for Mesh 3, including a zoomed-in view of the boundary region highlighting the boundary layers, are shown in Fig. 4. Observe that the outlet region is extended by a length of $L = 5D_{\text{outlet}}$ to minimize the influence of outlet boundary conditions on the flow within the nasal airways.

In Fig. 5, the velocity magnitude distribution is presented across the planes $S_0 - S_3$ for the four different meshes (M0–M3) considered. As observed, slight deviations are notable in the results obtained with $M0$ compared to $M1$, indicating a lack of sufficient resolution. However, from $M1 - M3$, the differences vanish, suggesting that most of the key flow features are already well captured by $M1$.

Next, we analyze the distribution of turbulent kinetic energy k in the $S_0 - S_3$ planes for all mesh resolutions considered, see Fig. 6, further supporting the evaluation of mesh sensitivity in this study.

As visualized, the deviations between $M0$ and $M1$ are most pronounced, indicating that $M0$ lacks the necessary resolution to capture the turbulent kinetic energy features accurately. In addition, while deviations between $M1$ and $M2$ are still notable across all planes (particularly pronounced in plane S_2, S_3), they are significantly less severe than those observed between the two coarsest meshes ($M0$, $M1$). The differences between $M2$ and $M3$ are overall minor, with $M2$ capturing most of the turbulent kinetic energy (and velocity magnitude) features. This demonstrates that $M2$ offers a good balance, achieving accurate results at a significantly lower computational cost than $M3$.

A supplementary comparison of velocity and turbulent kinetic energy profiles in the nasal cavity can be found in Appendix D. Considering the balance between accuracy and computational efficiency, $M2$ is selected for further analysis, as it sufficiently resolves both the velocity and turbulent kinetic energy within the nasal airways.

4.2. Flowfields

Airflow simulations within the nasal cavity are conducted under steady-state conditions across a range of breathing scenarios, with varying mass flow rates applied at the nostrils. In adult nasal airflow, a flow rate below 15 L/min generally results in laminar flow, characterized by Reynolds numbers typically less than 2000. When the flow

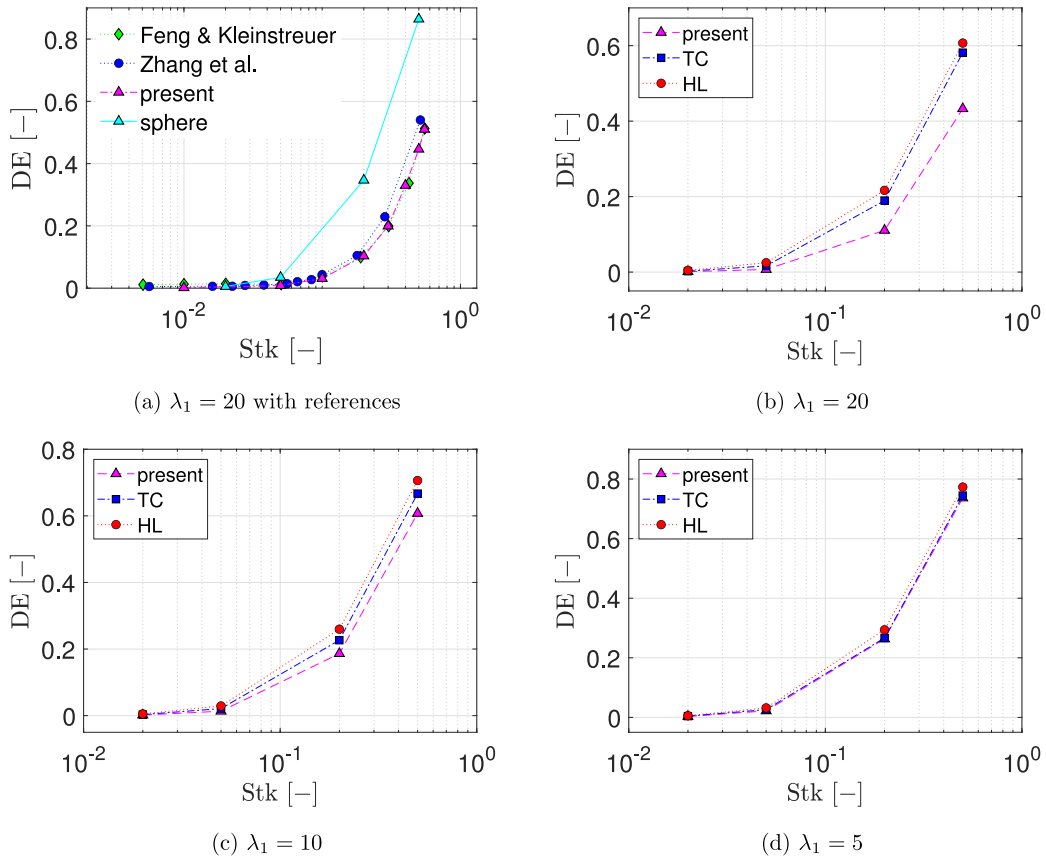


Fig. 3. Deposition efficiency DE [−] in a simplified bifurcation for prolate ellipsoids with $\lambda_1 = [5, 10, 20]$. Deposition efficiency DE is defined as the ratio of deposited particles to injected particles. ● Zhang et al. (1996), ◆ Feng and Kleinstreuer (2013), △ present model ($\lambda_1 = 20$) using EL-ER model, ▲ present model (sphere). Obtained results using shape factors: ● Haider & Levenspiel (HL) shape factor (Haider and Levenspiel, 1989), ■ Tran–Cong (TC) shape factor (Tran-Cong et al., 2004).

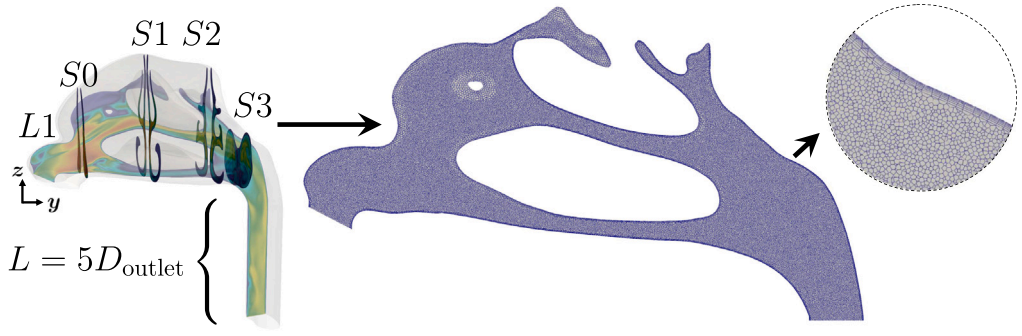


Fig. 4. Visualization of employed computational domain (M2) in the L1 plane. Slices from left to right: S0, S1, S2, S3. The slices S0–S3 possess a plane normal [0, 1, 0] and are defined using the following offset in streamwise position y [mm]: 19.4, 44.4, 69.4, 81.9. The left cross-sectional plane L1 is defined by the point [−0.005, 0, 0] and plane normal [1, 0, 0].

rate exceeds 15 L/min, the airflow becomes turbulent, as the Reynolds number surpasses 2000, Corda et al. (2024). Recall that in this work flow rates in the range of 7.5–30 L/min are considered. In Fig. 7, the contours of the mean velocity magnitude and turbulent kinetic energy are compared for the left cross-sectional plane L1, which is defined by the point [−0.005, 0, 0] and plane normal [1, 0, 0].

Fig. 7(a–c) illustrates the velocity and turbulent kinetic energy k distributions at flow rates of 7.5, 15, and 30 L/min in the left central plane of the nasal airways, respectively. As the flow rate increases, notable changes in the flow features are observed, including higher velocity magnitudes and more pronounced regions of turbulence, particularly in areas of complex geometry such as the frontal nasal airways.

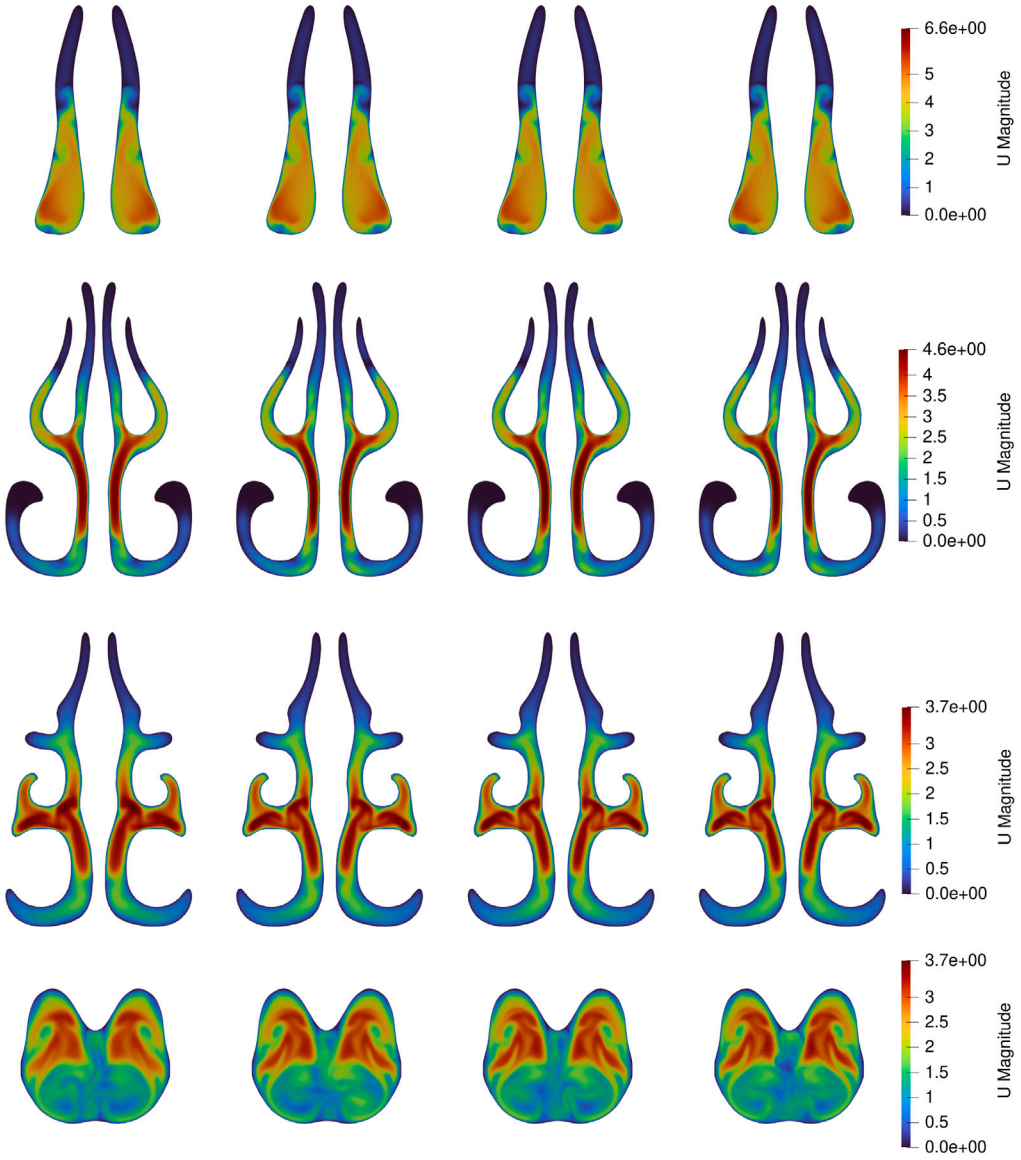


Fig. 5. Velocity magnitude U distribution in four selected planes. From left to right column: M0, M1, M2, M3. From top to bottom row: S0, S1, S2, S3. The slices S0–S3 are defined using the following offset in streamwise position y [mm]: 19.4, 44.4, 69.4, 81.9.

At 7.5 L/min, the flow remains mostly laminar with low k, while at 15 L/min and 30 L/min, the flow becomes increasingly turbulent, i.e. more elevated k levels and more spatially extensive turbulent structures.

Next, we evaluate the pressure drop ΔP, i.e., the (surface-averaged) pressure difference between the airway inlet and the end of the nasal septum as depicted in Fig. 8(b). Fig. 8(a) presents the resulting pressure drop over the flow rate Q (per nostril) alongside reference data from the literature. Note that although the literature employed a different nasal replica than the one used in the present study, the resulting pressure drop is within the reported range, and this qualitative agreement is a further indication of an appropriate numerical setup. Furthermore, the present results appear to fall between those reported for nasal models B (slightly smoothed) and C (more strongly smoothed) by Schroeter et al. (2011), which seems reasonable given that we employ an averaged geometry that, due to its creation process, is inherently smoother than an individual scanned geometry.

Likewise to Schroeter et al. (2011), we first fit the pressure drop ΔP [Pa] vs the flow rate Q $\left[\mathrm{m}^3/\mathrm{s}\right]$ using $\Delta P = aQ^b$ with $Q_{\mathrm{total}} = [3.5,\ 20]$ L/min. The resulting constants a and b, together with the reference results from Schroeter et al. are presented in Table 4

Similar to the findings of Schroeter et al. (2011), the exponents derived for the present CFD simulations were lower than the value of reported by Kelly et al. (2004a) using vitro measurements ($b = 1.83$). However, the resulting exponents are in the range of the reported results for five nasal replica casts by Garcia et al. (2009) ($b = 1.76$–1.87). As mentioned by Schroeter et al. (2011), the nasal models developed by Garcia et al. (2009) were constructed similarly to those of Kelly et al. (2004a) and exhibited comparable surface smoothness and wall roughness factors.

Despite these differences, the exponent b is close to the theoretical value of 1.75, suggesting that Eq. (33) remains a valid representation for estimating the characteristic diameter of the nasal cavity. Applying this equation, the characteristic diameter for the present model results as 6.94 mm (see Table 5). This value is consistent with the 5.5–7.3 mm

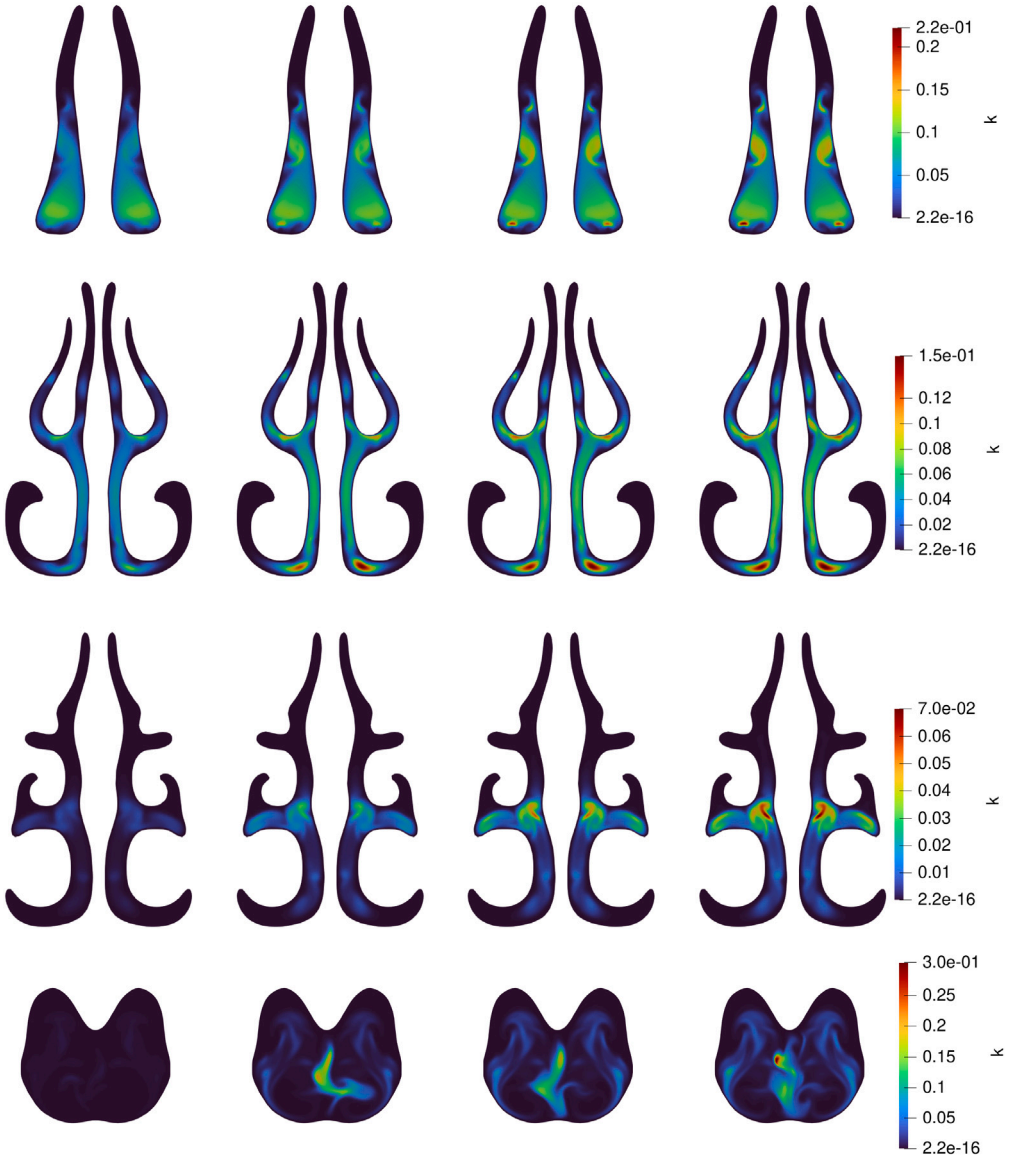


Fig. 6. Turbulent kinetic energy k profiles in four selected planes. From left to right column: M0, M1, M2, M3. From top to bottom row: S0, S1, S2, S3. The slices S0–S3 are defined using the following offset in streamwise position y [mm]: 19.4, 44.4, 69.4, 81.9.

Table 4
Pressure drop ΔP [Pa] versus flow rate (Q [m^3/s]. Employed fitting curve $\Delta P = aQ^b$, where $Q_{\text{total}} = [3.5,\ 20]$ L/min for the present model. The resulting constants a and b and the correlation coefficient r^2 are presented. Note that the $\pm$ values represent half the width of the 95% confidence interval for each fitted parameter.

Nasal replica/CFD Model	a	b	r^2
Kelly et al. (2004a,b)	$(5.7 \pm 0.8) \times 10^7$	1.83 ± 0.02	0.9994
Schroeter et al. (2011): Model A	$(1.1 \pm 0.2) \times 10^7$	1.64 ± 0.02	0.9996
Schroeter et al. (2011): Model B	$(0.32 \pm 0.04) \times 10^7$	1.49 ± 0.02	0.9996
Schroeter et al. (2011): Model C	$(0.43 \pm 0.15) \times 10^7$	1.57 ± 0.05	0.9976
present model	$(2.8 \pm 0.393) \times 10^7$	1.77 ± 0.017	0.9999

range previously reported for healthy nasal passages by Garcia et al. (2009).

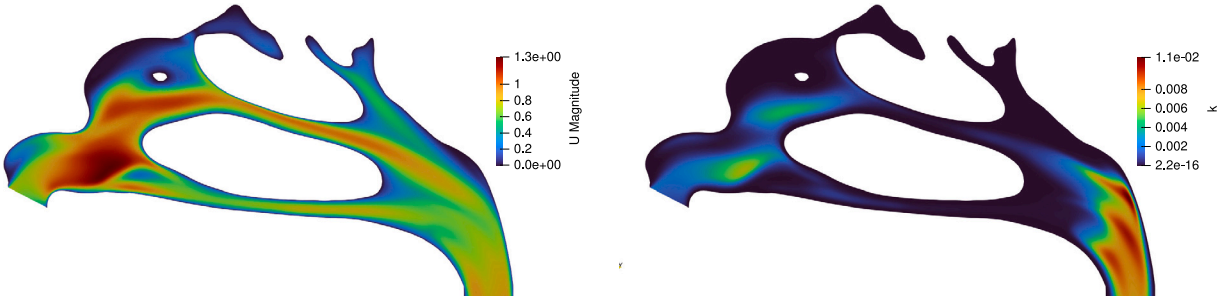
4.3. Particle deposition study

In the following, particle deposition in the nasal cavity is analyzed. In this context, we employ the deposition efficiency DE, which is defined as the ratio of the particles deposited at a specific region in the nasal airways to the total particle number injected:

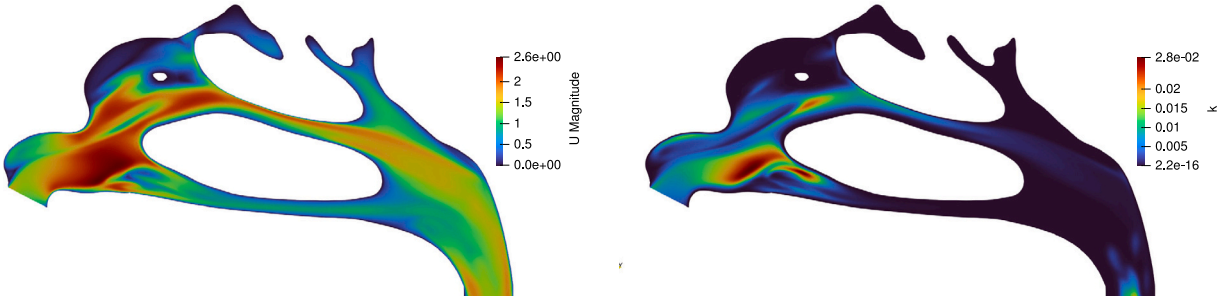
$$\text{DE} = \frac{\text{Number of particles deposited in specific region}}{\text{Total number of particles injected}}. \tag{36}$$

4.3.1. Spherical particles

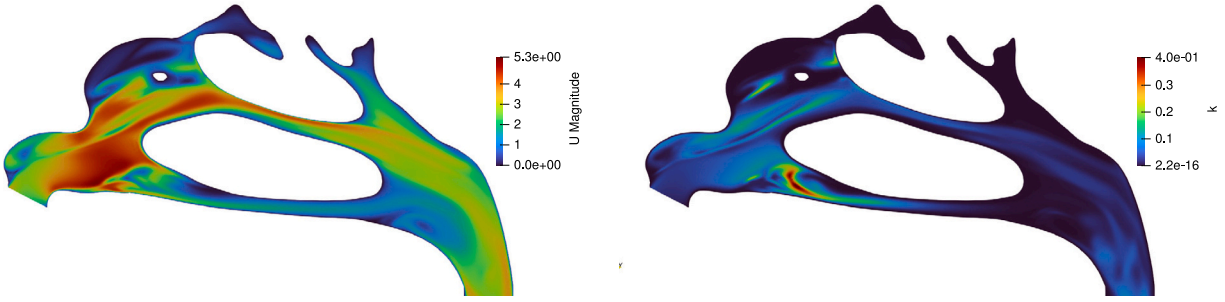
To validate the numerical model, we first compare the deposition efficiency of spherical micro-particles obtained in this study with experimental and numerical reference data from the literature (Kelly et al.,



(a) U (left) and k (right) distribution for $Q_{\text{total}} = 7.5\,\text{L/min}$

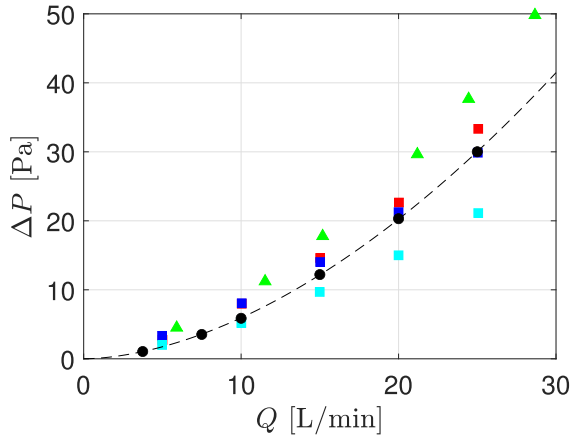


(b) U (left) and k (right) distribution for $Q_{\text{total}} = 15\,\text{L/min}$



(c) U (left) and k (right) distribution for $Q_{\text{total}} = 30\,\text{L/min}$

Fig. 7. Velocity magnitude U and turbulent kinetic energy k distribution in the L1 plane of the nasal airways. Displayed results for flow rates: 7.5, 15 and 30 L/min. (Note the different scaling employed for the different flow-rates).



(a) Pressure drop

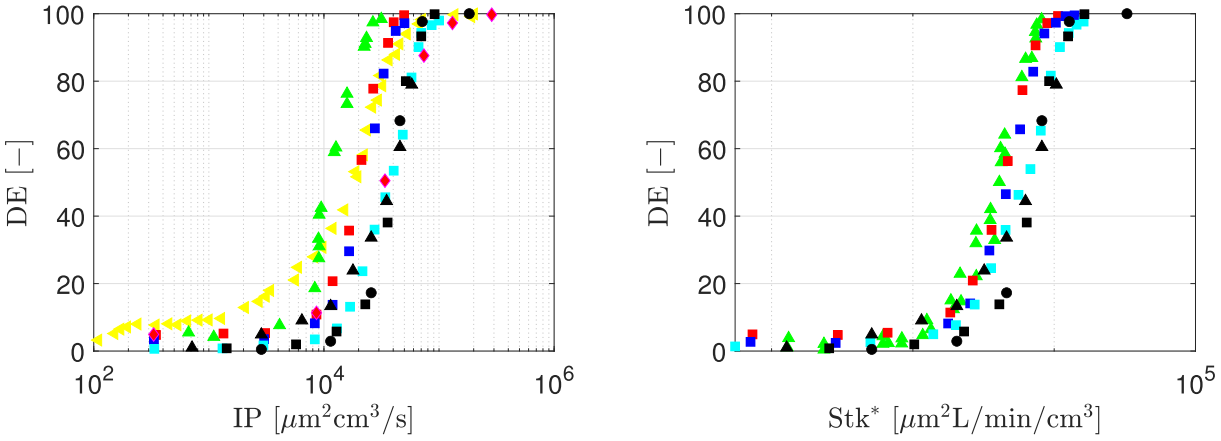


(b) Location of the representative nasal outlet patch

Fig. 8. Comparison of computed pressure drop through the nasal cavity from present RANS simulations with literature data: ●present, ▲Kelly et al. (2004a), ■Schroeter et al. (Model A) (Schroeter et al., 2011), ■Schroeter et al. (Model B) (Schroeter et al., 2011), ■Schroeter et al. (Model C) (Schroeter et al., 2011). Note that in the models of Schroeter et al. model B has a slightly smoothed nasal surface, whereas model C is more strongly smoothed.

Table 5
Characteristic diameter (D_c) of the nasal cavity calculated via Eq. (33) and length from the nostrils to the end of the septum (L_{nose}). The nasal resistance (R_{nose}) was calculated by fitting the pressure drop versus flow rate data with $\Delta p = R_{nose} Q^{1.75}$. The correlation coefficient of the fitting is denoted as r^2.

Nasal replica/CFD Model	D_c [cm]	L_{nose} [cm]	R_{nose} [Pa/[m^3/s]$^{1.75}$]	r^2
Schroeter et al. (2011): Model A	0.647	5.85	$(2.65 \pm 0.03) \times 10^7$	0.9978
Schroeter et al. (2011): Model B	0.667	5.85	$(2.30 \pm 0.05) \times 10^7$	0.9876
Schroeter et al. (2011): Model C	0.710	5.85	$(1.70 \pm 0.03) \times 10^7$	0.9921
present model	0.694	7.64	$(2.46 \pm 0.05) \times 10^7$	0.9959



(a) DE as a function of IP (b) DE as a function of Stk*

Fig. 9. Nasal deposition efficiency in a human airway replica as a function of the impaction parameter and flow rate. Investigated particle diameter d_{eq} for Q_{total} = 7.5 L/min: d_{eq} = [2.5, 5, 7.5, 10, 15, 17.5, 20, 22.5] μm, Q_{total} = 15 L/min: d_{eq} = [2.5, 5, 7.5, 10, 15, 17.5, 20] μm, Q_{total} = 30 L/min: d_{eq} = [2.5, 5, 7.5, 10, 20] μm). Presented data: ● present (Q_{total} = 30 L/min), ■ present (Q_{total} = 15 L/min), ▲ present (Q_{total} = 7.5 L/min), ▲ Kelly et al. (2004a), ■ Schroeter et al. (Model A) (Schroeter et al., 2011), ■ Schroeter et al. (Model B) (Schroeter et al., 2011), ■ Schroeter et al. (Model C) (Schroeter et al., 2011), ◆ Inthavong et al. (2011), ◀ Hsu and Chuang (2012).

2004a; Schroeter et al., 2011; Inthavong et al., 2011; Hsu and Chuang, 2012). The comparison is based on the impaction parameter IP, defined in Eq. (34) as the product of the squared particle aerosol diameter (d_a in mm^2) and the inhalation flow rate (Q in cm^3/s) per nostril.

In this context, we examine the deposition of microspheres with diameters ranging from 2.5 to 22.5 μm under different flow rates (Q_{total} = 7.5–30 L/min). Fig. 9(a) shows the deposition efficiency DE plotted against the impaction parameter IP, comparing the present results with literature data. As observed, the deposition predictions obtained in this study follow the characteristic sigmoidal trend: deposition fractions remain near 0% for 2.5 μm particles and rise sharply to nearly 100% for larger particle sizes ($d_{eq} \geq 12.5$ μm).

Overall, the predicted particle deposition lies within the range of values reported in the literature. The general trend shows strong agreement with previous studies, with discrepancies primarily attributed to anatomical variations in the nasal geometries employed. For Q_{total} = 15 L/min and 30 L/min, the present results collapse onto a single curve, indicating consistent behavior across these flow rates. In contrast, at Q_{total} = 7.5 L/min, noticeable deviations appear for IP $\leq 10^4$ [μm^{2}cm^3/s], which we attribute to pronounced differences in flow field characteristics within the nasal cavity (see Fig. 7). Overall, the predicted deposition values show the closest agreement with the results of Schroeter et al. (2011) (Model C).

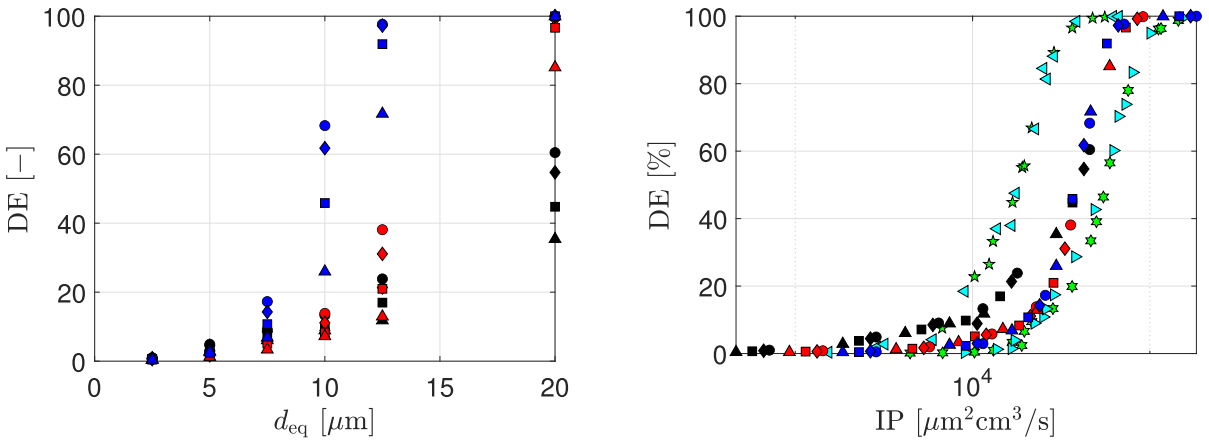
Next, we employ the characteristic nasal cavity length D_c to present the deposition efficiency (DE) as a function of the modified Stokes number, Stk*. Using Stk* instead of IP aims to correct the influence of anatomical variability across nasal models by normalizing the inertial parameter with D_c^3 (see Eq. (31)). In general, this normalization tends to collapse the DE curves of different models more closely, though notable discrepancies between them remain. Once again, the closest agreement is observed with the results of Schroeter et al. (2011) (Model C). For consistency, however, we adopt the uncorrected IP parameter in the subsequent comparisons, as it more directly reflects anatomical and flow-specific variations.

4.3.2. Ellipsoidal particles

Next, we investigate the deposition behavior of ellipsoidal particles, focusing on prolate ellipsoids, at the three flow rates considered in this study (7.5, 15, and 30 L/min). Fig. 10(a) presents the deposition efficiency (DE) as a function of the volume-equivalent diameter d_{eq}. As expected, DE increases markedly with flow rate. At the highest flow rate (Q_{total} = 30 L/min), particles of all considered shapes reach deposition efficiencies above 70% already at d_{eq} = 12.5 μm. In contrast, at the lowest flow rate (7.5 L/min), deposition remains considerably lower for all particle sizes studied, with strongly elongated particles (λ_1 = 10) remaining below 40% DE, compared to up to 60% for spherical particles.

Next, we compare our fiber deposition results with the findings of Dastan et al. (2014), who investigated fiber deposition in two nasal geometries (Model A and Model B). Their results shown in Fig. 10(b) indicate that, for a given geometry, deposition across different flow rates follows a unified sigmoid-like trend. In contrast, when comparing different geometries, the same sigmoid behavior is observed but shifted depending on the nasal anatomy.

Our results likewise produce a smooth sigmoid-shaped curve for the flow rates of Q_{total} = 15 L/min and 30 L/min. At 7.5 L/min, deposition still follows a sigmoid trend but does not collapse onto the same curve as the higher flow rates. This behavior is consistent with the spherical particle case (see Section 4.3.1) and is again attributed to altered flow dynamics in the nasal airway at low flow conditions. Overall, our



(a) DE as a function of d_{eq} (b) DE as a function of IP

Fig. 10. Nasal deposition efficiency in a human airway replica as a function of (a) the particle volume equivalent spherical diameter d_{eq} and (b) the Impaction parameter IP. Displayed Q_{total} [L/min]: 7.5, 15, 30. Displayed aspect ratio λ_1 for present model: $\lambda_1 = 1$ (sphere), $\lambda_1 = 2.5$, $\lambda_1 = 5$, $\lambda_1 = 10$. Displayed reference results Dastan et al. (2014) (Geometry A, $Q_{total} = 15$ L/min), Dastan et al. (2014) (Geometry A, $Q_{total} = 20$ L/min), Dastan et al. (2014) (Geometry B, $Q_{total} = 15$ L/min), Dastan et al. (2014) (Geometry B, $Q_{total} = 20$ L/min).

predicted deposition values fall within the range reported by Dastan et al. (2014).

For a more detailed analysis, Fig. 11(a–c) illustrates the dependence of DE on particle aspect ratio λ_1 at flow rates of (a) 7.5 L/min, (b) 15 L/min, and (c) 30 L/min. A consistent trend emerges across all flow conditions: increasing particle aspect ratio reduces DE, indicating that elongated (fibrous) particles are more likely to bypass nasal filtration and penetrate deeper into the respiratory tract. The influence of particle shape is most pronounced for intermediate particle sizes (7.5–12.5 µm), where DE is clearly sensitive to λ_1. For smaller particles (≤5 µm), the aspect ratio has little impact, as their low inertia allows them to follow the airflow streamlines and pass through the nasal cavity regardless of shape. At the other extreme, the largest particles considered (20 µm) show high deposition due to their inertia, with aspect ratio still exerting a measurable influence. Nevertheless, these large particles are efficiently filtered by the nasal airways, with DE approaching 100% for aspect ratios $\lambda_1 \leq 2.5$ at 15 L/min and for all shapes at 30 L/min, making them unlikely to penetrate deeper into the airway system.

To extend our analysis, we investigate how the key parameters — flow rate, particle size, and particle shape — affect local deposition patterns within the nasal cavity, with the aim of identifying regional hotspots. Specifically, we present results for total flow rates of $Q_{total} =$ 15 L/min and 30 L/min, considering particles with a volume-equivalent diameter of $d_{eq} = 10$ µm and three aspect ratios: $\lambda_1 = 2.5,\ 5$, and 10.

Our analysis reveals that, at a given flow rate, particle shape affects not only the overall DE but also the location and intensity of deposition hotspots. At $Q_{total} = 15$ L/min with $\lambda_1 = 2.5$, no hotspot is observed in the frontal nasal region near the nostrils, see Fig. 12(a). With increasing aspect ratio $\lambda_1 = 5$, a frontal hotspot begins to form, though with relatively low intensity, see Fig. 12(b). For $\lambda_1 = 10$, a pronounced hotspot emerges near the nostril inlet (see Fig. 12c). Interestingly, at the higher flow rate of $Q_{total} = 30$ L/min, the trend reverses, with frontal deposition hotspots diminishing as the aspect ratio increases.

Moreover, our results show that variations in flow rate (i.e., exercise level) strongly influence both the global DE and the spatial distribution of deposited particles for a given particle shape. This effect is particularly evident when comparing Fig. 12(a) with (d), (b) with (e), and (c) with (f), where distinctly different hotspot patterns emerge.

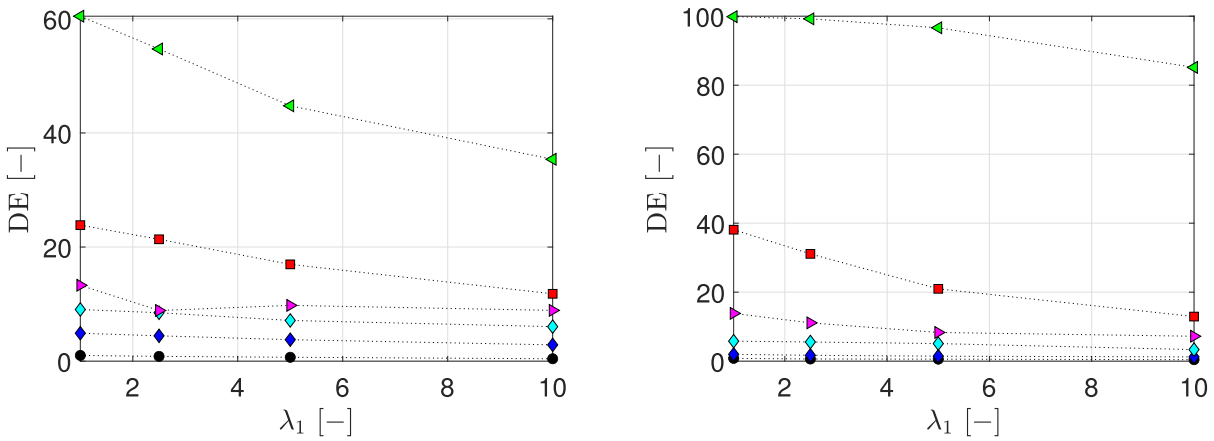
To better quantify and compare deposition intensity across different particle shapes, we visualize particle deposition using histograms along the lateral $\boldsymbol{x}$, streamwise $\boldsymbol{y}$, and gravitational $\boldsymbol{z}$ direction of the nasal cavity.

As illustrated in Fig. 13, the employed coordinate system is denoted by x, y, and z. The normalized spanwise coordinate is defined as $\hat{x} = x/L_x$, where $L_x = 29.9145$ mm is the maximum lateral extent of the nasal cavity. Similarly, $\hat{y} = y/L_y$ represents the normalized streamwise direction with $L_y = 99.2562$ mm as the maximum cavity length, and $\hat{z} = z/L_z$ denotes the normalized gravitational direction, with $L_z = 60.0432$ mm being the maximum cavity height (excluding the pipe extension).

We begin by analyzing the local particle deposition efficiency at $Q_{total} = 7.5$ L/min for particles with $d_{eq} = 7.5$–12.5 µm, considering both spherical particles ($\lambda_1 = 1$) and fibrous particles with aspect ratios $\lambda_1 = 5$ and $\lambda_1 = 10$. The results show that the spatial distribution of deposited particles depends strongly on particle size (see, e.g., Fig. 14(a,d,g), or likewise (b,e,h) and (c,f,i)). Moreover, deposition hotspot intensity decreases with increasing particle elongation ($\lambda \uparrow$), suggesting that elongated particles can bypass the nasal filtering mechanism more effectively and penetrate deeper into the airways. This, in turn, results in a reduction of the total deposition efficiency (DE) for particles with larger aspect ratios, as shown in Fig. 11.

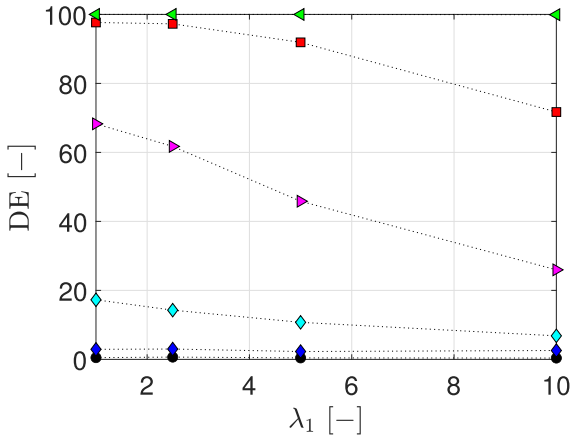
We also observe that the mean deposition location shifts in both the $\hat{y}$ and $\hat{z}$ directions. Along $\hat{y}$, hotspots progressively move towards the rear of the nasal cavity with increasing λ. In the $\hat{z}$ direction, a notable shift towards lower values is found for $d_{eq} = 10$ µm, as particle deposition in the range $\hat{z} \in [0.6, 0.8]$ decreases significantly. For $d_{eq} =$ 7.5 µm and $d_{eq} = 12.5$ µm, however, the changes in mean deposition with increased aspect ratio are less pronounced.

Next, we investigate the local particle deposition efficiency at an increased flow rate of $Q_{total} = 15$ L/min (see Fig. 15). Compared to 7.5 L/min (as presented in Fig. 14), the deposition patterns change markedly. At the lower flow rate, deposited particles are more broadly distributed across $\hat{x}$, $\hat{y}$, and $\hat{z}$, whereas at 15 L/min the hotspots become more distinct. Note that again, the distribution of deposited particles depends significantly on the particle size considered. Consistent with the observations at 7.5 L/min (see Fig. 14), we find that the deposition hotspot intensity decreases markedly in all directions with increasing particle elongation. In addition, the mean deposition location shifts noticeably along both the $\hat{y}$ and $\hat{z}$ axes. Contrastingly to 7.5 L/min, in the case of 15 L/min, increasing λ_1 shifts the mean particle deposition location in $\hat{y}$ further towards the front of the nasal cavity as the



(a) DE over λ_1 ($Q_{\text{total}} = 7.5\,\text{L/min}$)

(b) DE over λ_1 ($Q_{\text{total}} = 15\,\text{L/min}$)



(c) DE over λ_1 ($Q_{\text{total}} = 30\,\text{L/min}$)

Fig. 11. Deposition efficiency in a human nasal replica as a function of the volume equivalent spherical diameter d_{eq}, the particle aspect ratio λ_1, and flow rate Q_{total}. Investigated particle diameter in [µm]: ◂ 20, ■ 12.5, ▸ 10, ◆ 7.5, ◆ 5, ● 2.5.

deposition hotspots in the center and rear of the nasal cavity decrease significantly. Along $\hat{z}$, we find that for $d_{\text{eq}} = 7.5 - 10\,\mu\text{m}$ an increase in aspect ratio leads to a decreased deposition in the upper nasal cavity, shifting the mean deposition towards lower $\hat{z}$ values. For $d_{\text{eq}} = 12.5\,\mu\text{m}$, a similar reduction of deposition in the upper airways is observed with increased aspect ratio. Nevertheless, the mean deposition shifts slightly upward, since particle deposition in the range $\hat{z} \in [0.2, 0.4]$ decreases strongly.

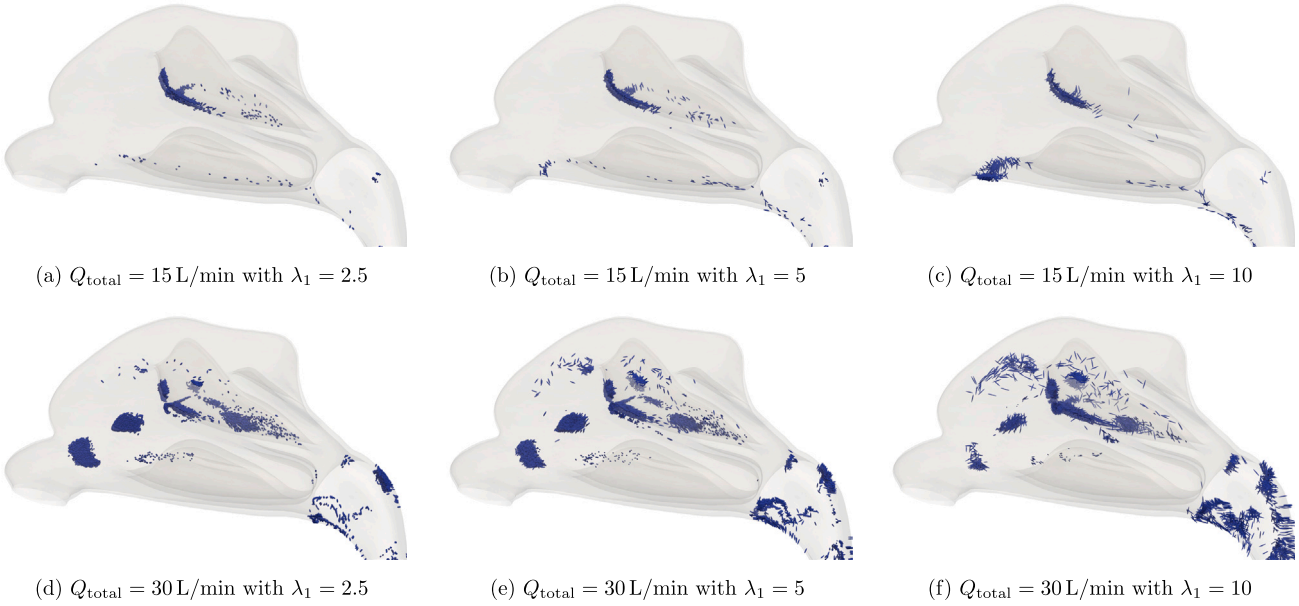
Finally, we analyze the local particle deposition efficiency at the highest flow rate considered, i.e. $Q_{\text{total}} = 30\,\text{L/min}$ (see Fig. 16). Increasing the flow rate from 15 to 30 L/min produces substantial changes in deposition patterns, with hotspots becoming more intense at higher flow rates. The distribution of these hotspots is also strongly influenced by the particle diameter d_{eq}. Consistent with the observations at lower flow rates (see Fig. 14 and Fig. 15), hotspot intensity decreases notably.

In the $\hat{x}$ direction (Fig. 16(a,d,g)), this reduction is evident across all particle sizes, where increasing aspect ratio diminishes deposition along the inner nasal cavity walls. Furthermore, the mean particle deposition shifts markedly in both $\hat{y}$ and $\hat{z}$. As in the 7.5 L/min case, increasing λ_1 shifts deposition along $\hat{y}$ further towards the rear of the nasal cavity. In the $\hat{z}$ direction, however, the effect depends on particle size: for $d_{\text{eq}} = 12.5\,\mu\text{m}$, elongated particles preferentially deposit in the upper airways ($\hat{z} \geq 0.58$), whereas for smaller particles, increasing aspect ratio reduces deposition in this region.

4.3.3. Comparison to shape factors

Lastly, we evaluate the performance of shape-factor-based approaches. Deposition efficiency (DE) is compared at two flow rates (15 L/min and 30 L/min) using either the present EL-ER approach, which explicitly accounts for shape-dependent particle rotation, or simplified methods that approximate non-sphericity by applying shape factors (HL Haider and Levenspiel, 1989 and TC Tran-Cong et al., 2004) to spherical particles. The analysis considers three particle diameters ($d_{\text{eq}} = 7.5, 10, 12.5\,\mu\text{m}$) and aspect ratios ranging from $\lambda_1 = 1$–10. As shown in Fig. 17, shape-factor-based models fail to capture the overall DE trends: they underpredict deposition for moderately elongated particles ($\lambda_1 = 2.5$) and overpredict it for highly elongated particles ($\lambda_1 = 10$). Among the two, the TC-based correction provides closer agreement with the EL-ER approach, although discrepancies of up to 10% remain in the case of strongly elongated particles ($\lambda_1 = 10$).

To visualize particle deposition, Fig. 18 shows the local particle patterns at $Q_{\text{total}} = 15\,\text{L/min}$. The results indicate that shape-factor-based approaches not only fail to reproduce the overall DE for elongated particles ($\lambda_1 = 10$), but also do not accurately capture the location and intensity of deposition hotspots. For example, for $d_{\text{eq}} = 10\,\mu\text{m}$, both HL and TC corrections miss the frontal hotspot predicted by the EL-ER approach (Fig. 18(a–c)). Contrastingly, for $d_{\text{eq}} = 12.5\,\mu\text{m}$, deposition in the frontal cavity is overestimated by both shape-factor models compared to EL-ER approach, see Fig. 18(d–f).



(a) $Q_{\text{total}} = 15\,\text{L/min}$ with $\lambda_1 = 2.5$ (b) $Q_{\text{total}} = 15\,\text{L/min}$ with $\lambda_1 = 5$ (c) $Q_{\text{total}} = 15\,\text{L/min}$ with $\lambda_1 = 10$

(d) $Q_{\text{total}} = 30\,\text{L/min}$ with $\lambda_1 = 2.5$ (e) $Q_{\text{total}} = 30\,\text{L/min}$ with $\lambda_1 = 5$ (f) $Q_{\text{total}} = 30\,\text{L/min}$ with $\lambda_1 = 10$

Fig. 12. Particle deposition in the averaged nasal airway geometry for (a,b, c) $Q_{\text{total}} = 15\,\text{L/min}$ and (d,e, f) $Q_{\text{total}} = 30\,\text{L/min}$ for different particle aspect ratios λ_1. Particles considered are $d_{\text{eq}} = 10\,\mu\text{m}$. Particle scaling for visualization: 50×.

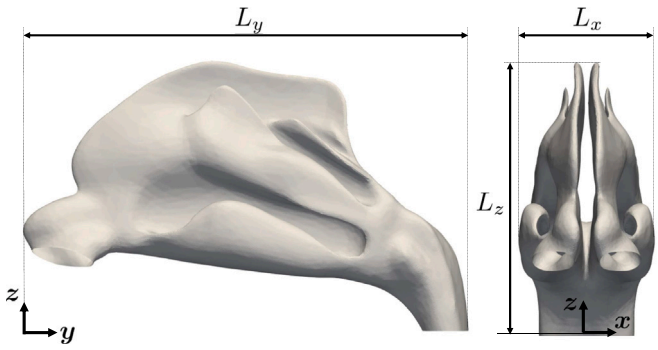


Fig. 13. Sketch of the coordinate system employed for the nasal cavity studied with maximum lateral extent L_x of the nasal cavity, maximum cavity length L_y and maximum cavity height L_z (excluding the pipe extension).

Fig. 19 presents the local particle deposition at $Q_{\text{total}} = 30\,\text{L/min}$. Once again, clear discrepancies emerge: shape-factor-based models overestimate deposition in the frontal region of the nasal cavity for both particle sizes considered ($d_{\text{eq}} = 7.5\,\mu\text{m}$ and $d_{\text{eq}} = 10\,\mu\text{m}$).

For a quantitative analysis of local deposition, we present histograms of particle deposition along $\hat{x}$, $\hat{y}$, and $\hat{z}$ for all considered models (HL Haider and Levenspiel, 1989, TC Tran-Cong et al., 2004, and EL-ER approach) for particles with $\lambda_1 = 10$. We begin with the case $Q_{\text{total}} = 15\,\text{L/min}$, see Fig. 20. The results show that, across all displayed particle sizes ($d_{\text{eq}} = 7.5$–$12.5\,\mu\text{m}$), employing shape factors yields substantial differences compared to the EL-ER approach. Both the intensity of deposition hotspots and the overall spatial distribution are altered. Notably, the HL model (Haider and Levenspiel, 1989) deviates most strongly from EL-ER approach, tending to overpredict deposition in hotspots. The TC model (Tran-Cong et al., 2004), while closer to the present EL-ER approach, still notably overestimates deposition in most hotspot regions.

When turning to the deposition patterns obtained at $Q_{\text{total}} = 30\,\text{L/min}$ (see Fig. 21), we observe a similar behavior. Both shape-factor models strongly overpredict deposition hotspots, with the TC model (Tran-Cong et al., 2004) performing slightly better than the HL model (Haider and Levenspiel, 1989). This again underlines that, beyond estimating total deposition efficiency for ellipsoidal particles, accurately capturing the spatial distribution of deposited particles requires accounting for non-sphericity via the EL-ER approach.

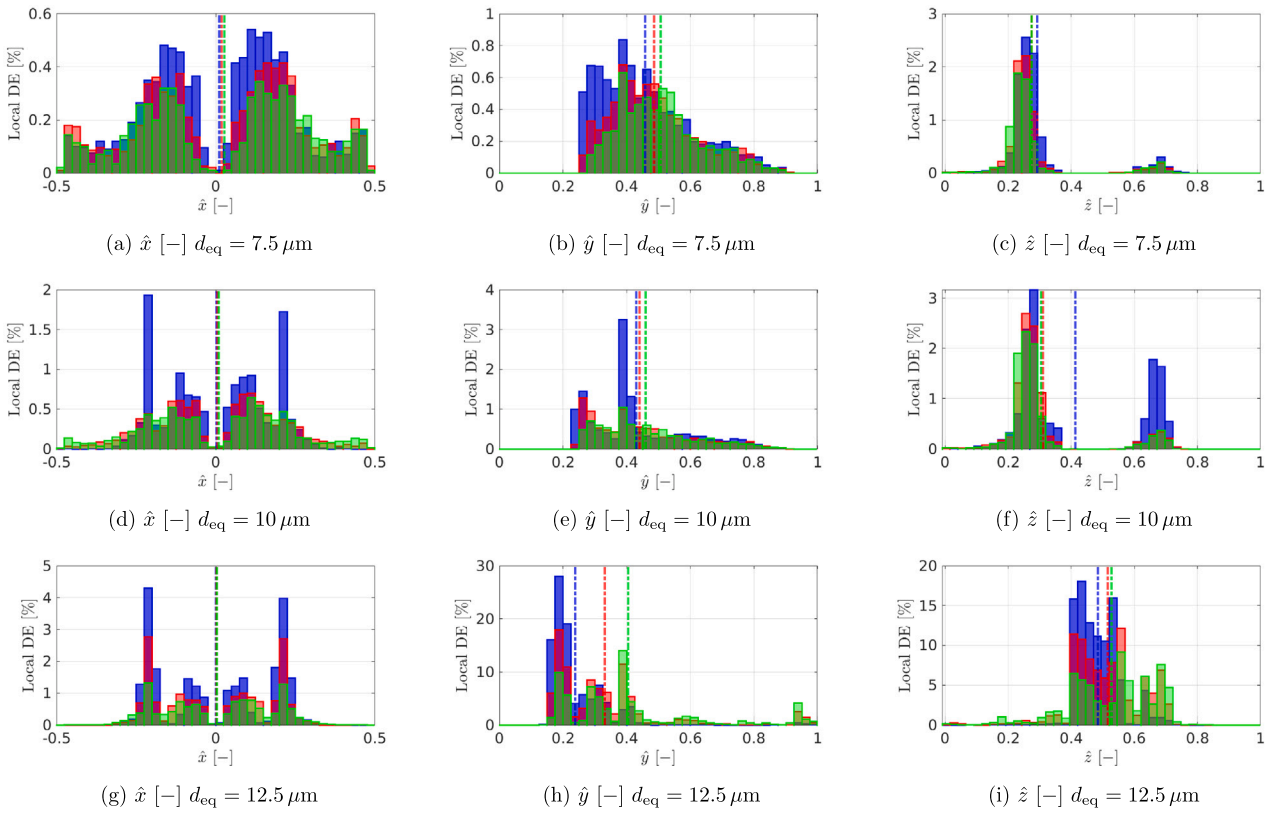
In summary, for strongly elongated particles ($\lambda_1 = 10$), we observe pronounced deviations in both total deposition efficiency and regional deposition when using the shape-factor models (TC, HL) compared to the EL-ER approach in the studied complex nasal airway geometry. Recall the simple bifurcation (Fig. 3, Section 3.4), where the shape-factor and EL-ER models agreed well for smaller aspect ratios ($\lambda_1 = 5$), but already fail for larger aspect ratios.

5. Conclusions

In this study, we employed the open-source software OpenFOAM to investigate ellipsoidal particle deposition in an averaged human nasal cavity replica. Simulations were carried out for different inhalation levels ranging from rest to moderate exercise, corresponding to total flow rates of 7.5 L/min, 15 L/min, and 30 L/min. A physiologically relevant particle size range of $d_{\text{eq}} = 2.5$–$20\,\mu\text{m}$ was considered, including both spherical ($\lambda_1 = 1$) and prolate ellipsoidal particles with aspect ratios $\lambda_1 = 2.5,\ 5,\ 10$. The simulations were performed using a frozen flow-field approach consistent with our previous works (see Wedel et al., 2021b,a), where the computational model is based on the RANS equations with a k–ω SST turbulence closure.

Our main findings can be summarized as follows

- By validating the EL-ER approach using a simple bifurcation geometry, we obtained good agreement with reference results. Even in this simplified setup, we observed pronounced deviations that emerged between the EL-ER approach and simplified shape-factor approaches, particularly for highly elongated particles.
- For the averaged nasal cavity, the simulated pressure drop across the geometry falls within the range reported in the literature. The predicted overall deposition efficiency (DE) also agrees well with both experimental and numerical reference data for spherical and



(a) $\hat{x}$ [−] $d_{\mathrm{eq}} = 7.5\,\mu\mathrm{m}$ (b) $\hat{y}$ [−] $d_{\mathrm{eq}} = 7.5\,\mu\mathrm{m}$ (c) $\hat{z}$ [−] $d_{\mathrm{eq}} = 7.5\,\mu\mathrm{m}$

(d) $\hat{x}$ [−] $d_{\mathrm{eq}} = 10\,\mu\mathrm{m}$ (e) $\hat{y}$ [−] $d_{\mathrm{eq}} = 10\,\mu\mathrm{m}$ (f) $\hat{z}$ [−] $d_{\mathrm{eq}} = 10\,\mu\mathrm{m}$

(g) $\hat{x}$ [−] $d_{\mathrm{eq}} = 12.5\,\mu\mathrm{m}$ (h) $\hat{y}$ [−] $d_{\mathrm{eq}} = 12.5\,\mu\mathrm{m}$ (i) $\hat{z}$ [−] $d_{\mathrm{eq}} = 12.5\,\mu\mathrm{m}$

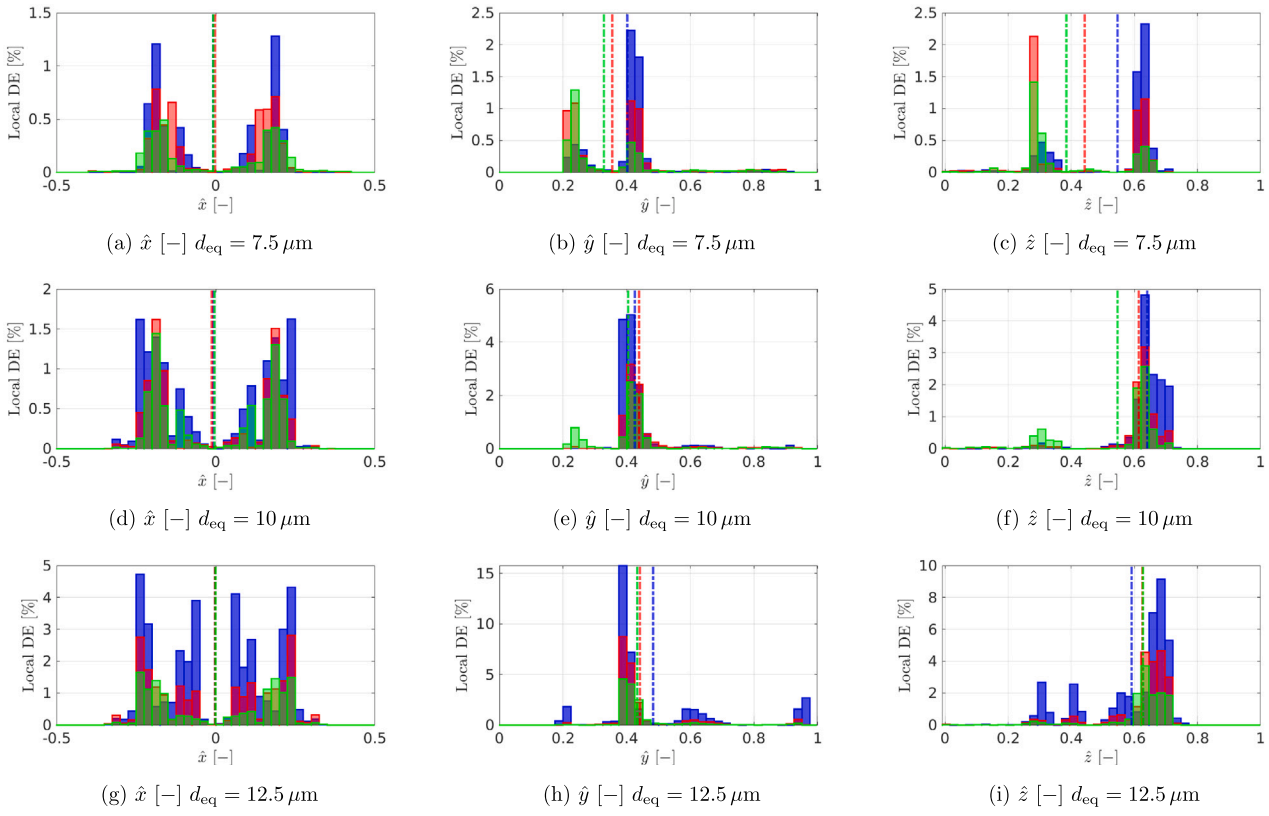
Fig. 14. Local DE for $Q_{\mathrm{total}} = 7.5\,\mathrm{L/min}$ for (a,b, c) $d_{\mathrm{eq}} = 7.5\,\mu\mathrm{m}$, (d,e, f) $d_{\mathrm{eq}} = 10\,\mu\mathrm{m}$ and (g,h, i) $d_{\mathrm{eq}} = 12.5\,\mu\mathrm{m}$ for different particle aspect ratios λ_1: 1, 5, 10. The mean is displayed using the presented color scheme and the line-style.

ellipsoidal particles, confirming that the averaged nasal airway is suitable for deposition studies. When DE is plotted against the inertial parameter (IP), the results for 15 L/min and 30 L/min collapse onto a common sigmoid-like curve, consistent with earlier findings.

- At 7.5 L/min, deviations in flow features were observed compared to higher flow rates. At 15 L/min and 30 L/min, the flow patterns were qualitatively similar, differing mainly in intensity. This was reflected in particle deposition: 15 L/min and 30 L/min mapped onto a common sigmoid curve when plotted over IP, while deviations appeared at 7.5 L/min, likely due to altered flow features.
- Flow rates were found to significantly influence deposition hotspots and the regional distribution of deposited particles. Higher inhalation rates resulted in more pronounced deposition hotspots and altered spatial deposition patterns.
- Both particle size and shape strongly influenced deposition efficiency. Larger particles were more likely to deposit due to inertial impaction, whereas smaller particles tended to follow the flow more closely and penetrate deeper into the lungs. For all studied flow rates and sizes, elongated fibers exhibited reduced overall deposition compared to spherical particles, thereby increasing the fraction of particles capable of reaching deeper lung regions and potentially causing disease.
- Substantial variability in regional deposition was observed between the simplified shape-factor models considered (HL Haider and Levenspiel, 1989 and TC Tran-Cong et al., 2004) and the EL-ER approach. Differences were not limited to overall deposition efficiency but also significant at the local scale, where spatial deposition patterns were strongly modified by the choice of model. In this context, we find that shape factors for strongly elongated particles lead to a notable overprediciton of particle deposition in the nasal cavity studied. This highlights the necessity of accurately capturing particle dynamics in the respiratory tract to derive reliable deposition trends.
- Between the two shape-factor models, we observed that TC (Tran-Cong et al., 2004) performed slightly better than HL (Haider and Levenspiel, 1989), yet both consistently overpredicted total deposition efficiency for elongated particles ($\lambda_1 = 10$) and misrepresented spatial deposition patterns.

In conclusion, our results demonstrate the critical importance of accurately modeling the dynamics of non-spherical, specifically ellipsoidal, particles in inhalation flows. Simplified shape-factor approaches fail to capture essential deposition trends and can lead to substantial misrepresentations of local deposition patterns. Such inaccuracies are not merely of academic concern: mispredicted spatial deposition could lead health professionals to underestimate particle penetration into the lower airways, misjudge drug delivery efficiency, or overlook regions particularly susceptible to harmful exposure.

Future work will aim to extend this analysis to transient breathing conditions and employ hybrid RANS–LES turbulence models, such as k–ω SST-DES, to further improve flow and deposition predictions.

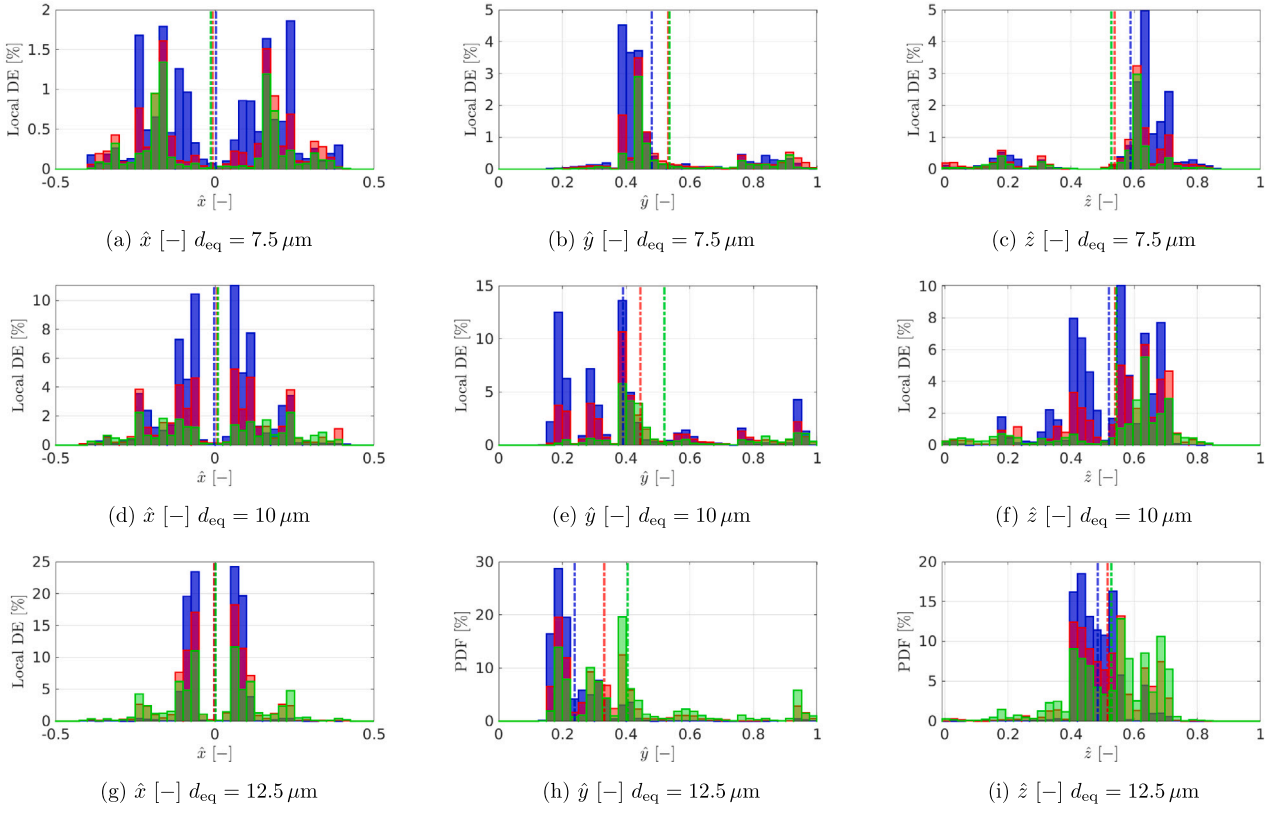


(a) $\hat{x}$ [−] $d_{eq} = 7.5\,\mu m$ (b) $\hat{y}$ [−] $d_{eq} = 7.5\,\mu m$ (c) $\hat{z}$ [−] $d_{eq} = 7.5\,\mu m$

(d) $\hat{x}$ [−] $d_{eq} = 10\,\mu m$ (e) $\hat{y}$ [−] $d_{eq} = 10\,\mu m$ (f) $\hat{z}$ [−] $d_{eq} = 10\,\mu m$

(g) $\hat{x}$ [−] $d_{eq} = 12.5\,\mu m$ (h) $\hat{y}$ [−] $d_{eq} = 12.5\,\mu m$ (i) $\hat{z}$ [−] $d_{eq} = 12.5\,\mu m$

Fig. 15. Local DE for $Q_{total} = 15$ L/min for (a,b, c) $d_{eq} = 7.5\,\mu m$, (d,e, f) $d_{eq} = 10\,\mu m$ and (g,h, i) $d_{eq} = 12.5\,\mu m$ for different particle aspect ratios λ_1: 1, 5, 10. The mean is displayed using the presented color scheme and the ▪▪ line-style.

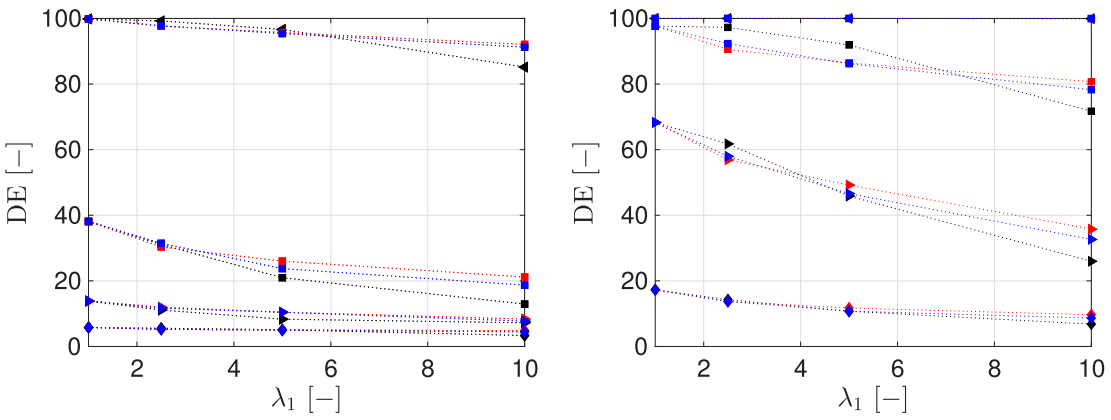


(a) $\hat{x}$ [−] $d_{eq} = 7.5\,\mu m$ (b) $\hat{y}$ [−] $d_{eq} = 7.5\,\mu m$ (c) $\hat{z}$ [−] $d_{eq} = 7.5\,\mu m$

(d) $\hat{x}$ [−] $d_{eq} = 10\,\mu m$ (e) $\hat{y}$ [−] $d_{eq} = 10\,\mu m$ (f) $\hat{z}$ [−] $d_{eq} = 10\,\mu m$

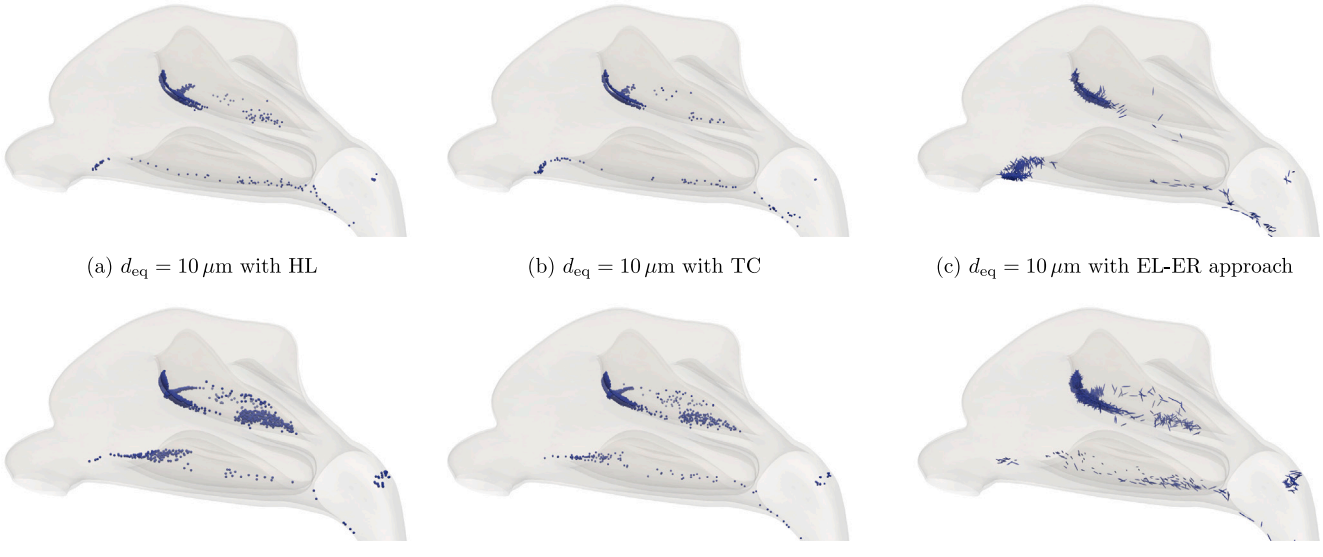
(g) $\hat{x}$ [−] $d_{eq} = 12.5\,\mu m$ (h) $\hat{y}$ [−] $d_{eq} = 12.5\,\mu m$ (i) $\hat{z}$ [−] $d_{eq} = 12.5\,\mu m$

Fig. 16. Local DE for $Q_{total} = 30$ L/min for (a,b, c) $d_{eq} = 7.5\,\mu m$, (d,e, f) $d_{eq} = 10\,\mu m$ and (g,h, i) $d_{eq} = 12.5\,\mu m$ for different particle aspect ratios λ_1: 1, 5, 10. The mean is displayed using the presented color scheme and the ▪▪ line-style.



(a) $Q_{\text{total}} = 15\,\text{L/min}$ (b) $Q_{\text{total}} = 30\,\text{L/min}$

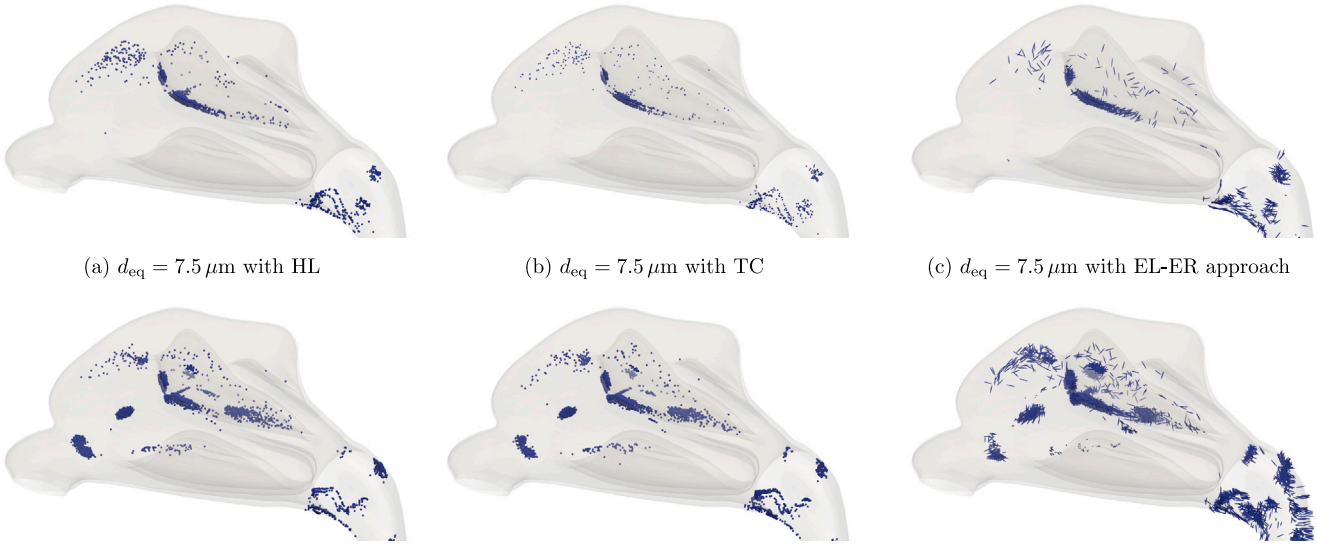
Fig. 17. Nasal deposition efficiency in a human airway replica as a function of the particle volume equivalent spherical diameter d_{eq}, the particle aspect ratio λ_1, and flow rate Q_{total} (a) 15 L/min and (b) 30 L/min. Investigated models: ▬ present approach (EL-ER), ▬ HL, ▬ TC. Investigated particle diameter in [μm]: ◂ 20 ■ 12.5, ▸ 10, ◆ 7.5.



(a) $d_{\text{eq}} = 10\,\mu\text{m}$ with HL (b) $d_{\text{eq}} = 10\,\mu\text{m}$ with TC (c) $d_{\text{eq}} = 10\,\mu\text{m}$ with EL-ER approach

(d) $d_{\text{eq}} = 12.5\,\mu\text{m}$ with HL (e) $d_{\text{eq}} = 12.5\,\mu\text{m}$ with TC (f) $d_{\text{eq}} = 12.5\,\mu\text{m}$ with EL-ER approach

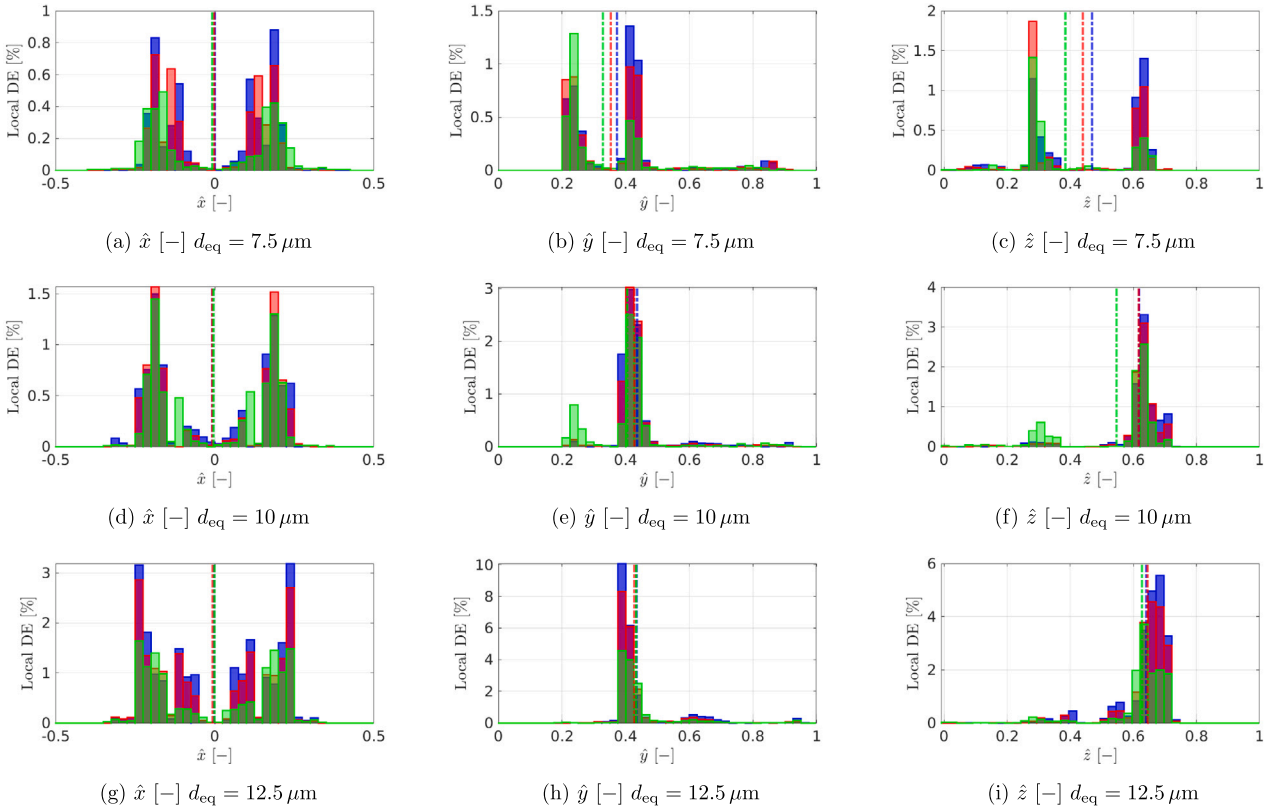
Fig. 18. Particle deposition in the nasal cavity for $Q_{\text{total}} = 15\,\text{L/min}$. Particles considered are $d_{\text{eq}} = 10\,\mu\text{m}$ and $d_{\text{eq}} = 12.5\,\mu\text{m}$ with $\lambda_1 = 10$. Particles are simulated using either HL (Haider and Levenspiel, 1989) or TC (Tran-Cong et al., 2004) shape factor or EL-ER approach. Particle scaling for visualization: 50× for $d_{\text{eq}} = 10\,\mu\text{m}$, 40× for $d_{\text{eq}} = 12.5\,\mu\text{m}$.



(a) $d_{eq} = 7.5\,\mu$m with HL (b) $d_{eq} = 7.5\,\mu$m with TC (c) $d_{eq} = 7.5\,\mu$m with EL-ER approach

(d) $d_{eq} = 10\,\mu$m with HL (e) $d_{eq} = 10\,\mu$m with TC (f) $d_{eq} = 10\,\mu$m with EL-ER approach

Fig. 19. Particle deposition in the nasal cavity for $Q_{total} = 30$ L/min. Particles considered are $d_{eq} = 7.5\,\mu$m and $d_{eq} = 10\,\mu$m with $\lambda_1 = 10$. Particles are simulated using either HL shape factor, TC shape factor or EL-ER approach. Particles are simulated using either HL (Haider and Levenspiel, 1989) TC (Tran-Cong et al., 2004) shape factor or EL-ER approach. Particle scaling for visualization: 50× for $d_{eq} = 10\,\mu$m, 66.667× for $d_{eq} = 7.5\,\mu$m.

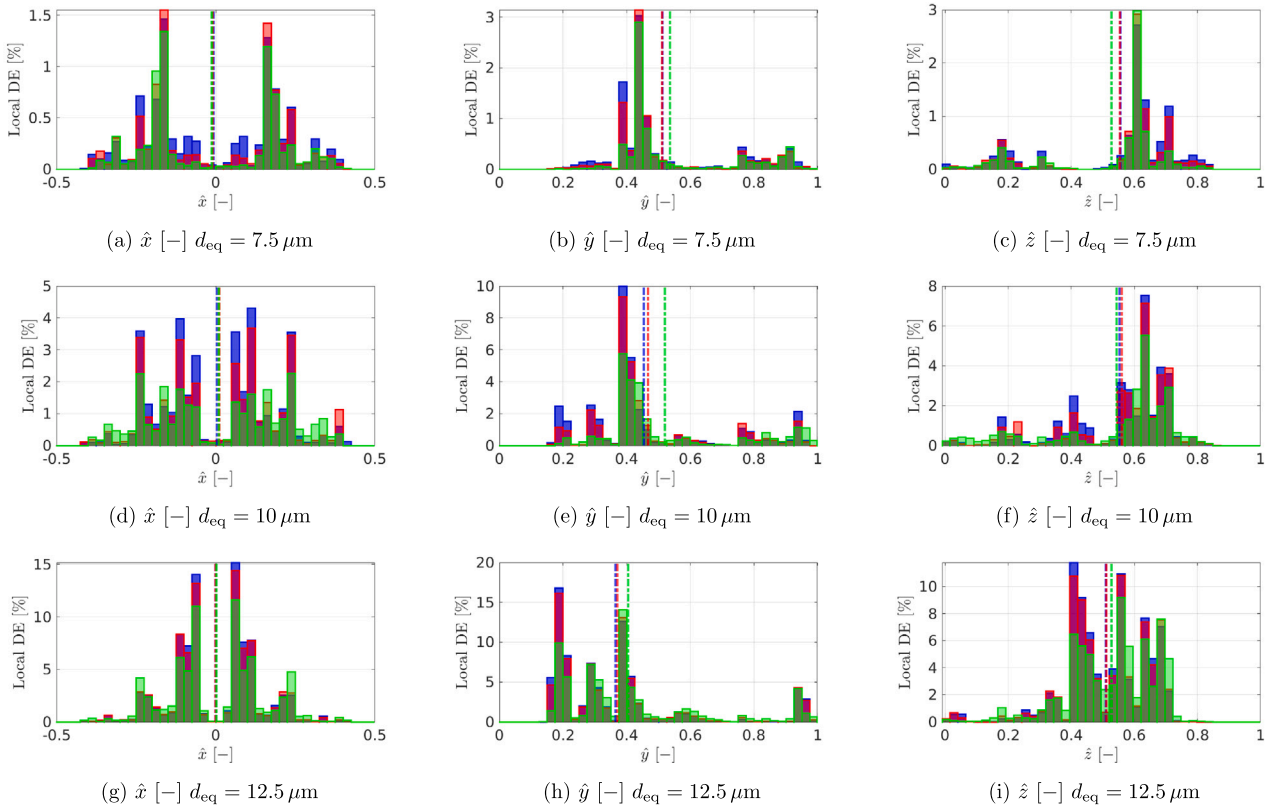


(a) $\hat{x}$ [−] $d_{eq} = 7.5\,\mu$m (b) $\hat{y}$ [−] $d_{eq} = 7.5\,\mu$m (c) $\hat{z}$ [−] $d_{eq} = 7.5\,\mu$m

(d) $\hat{x}$ [−] $d_{eq} = 10\,\mu$m (e) $\hat{y}$ [−] $d_{eq} = 10\,\mu$m (f) $\hat{z}$ [−] $d_{eq} = 10\,\mu$m

(g) $\hat{x}$ [−] $d_{eq} = 12.5\,\mu$m (h) $\hat{y}$ [−] $d_{eq} = 12.5\,\mu$m (i) $\hat{z}$ [−] $d_{eq} = 12.5\,\mu$m

Fig. 20. Local DE for $Q_{total} = 15$ L/min for (a, b, c) $d_{eq} = 7.5\,\mu$m, (d, e, f) $d_{eq} = 10\,\mu$m and (g, h, i) $d_{eq} = 12.5\,\mu$m for $\lambda_1 = 10$. Investigated models: HL (Haider and Levenspiel, 1989), TC (Tran-Cong et al., 2004), EL-ER approach. The mean is displayed using the presented color scheme and the line-style.



(a) $\hat{x}$ [−] $d_{\mathrm{eq}} = 7.5\,\mu\mathrm{m}$ (b) $\hat{y}$ [−] $d_{\mathrm{eq}} = 7.5\,\mu\mathrm{m}$ (c) $\hat{z}$ [−] $d_{\mathrm{eq}} = 7.5\,\mu\mathrm{m}$

(d) $\hat{x}$ [−] $d_{\mathrm{eq}} = 10\,\mu\mathrm{m}$ (e) $\hat{y}$ [−] $d_{\mathrm{eq}} = 10\,\mu\mathrm{m}$ (f) $\hat{z}$ [−] $d_{\mathrm{eq}} = 10\,\mu\mathrm{m}$

(g) $\hat{x}$ [−] $d_{\mathrm{eq}} = 12.5\,\mu\mathrm{m}$ (h) $\hat{y}$ [−] $d_{\mathrm{eq}} = 12.5\,\mu\mathrm{m}$ (i) $\hat{z}$ [−] $d_{\mathrm{eq}} = 12.5\,\mu\mathrm{m}$

Fig. 21. Local DE for $Q_{\mathrm{total}} = 30\,\mathrm{L/min}$ for (a,b, c) $d_{\mathrm{eq}} = 7.5\,\mu\mathrm{m}$, (d,e, f) $d_{\mathrm{eq}} = 10\,\mu\mathrm{m}$ and (g,h), (i) $d_{\mathrm{eq}} = 12.5\,\mu\mathrm{m}$ for $\lambda_1 = 10$. Investigated models: HL (Haider and Levenspiel, 1989), TC (Tran-Cong et al., 2004), EL-ER approach. The mean is displayed using the presented color scheme and the line-style.

CRediT authorship contribution statement

Jana Wedel: Writing – original draft, Visualization, Validation, Software, Methodology, Investigation, Formal analysis, Data curation, Conceptualization. **Nicolás Catalán:** Writing – original draft, Visualization, Validation, Investigation, Data curation, Conceptualization. **Paul Steinmann:** Writing – review & editing, Supervision, Resources, Project administration, Funding acquisition, Conceptualization. **Matjaž Hriberšek:** Writing – review & editing, Supervision, Resources, Project administration, Funding acquisition, Conceptualization. **Salvatore Cito:** Writing – review & editing, Supervision. **Sylvana Varela:** Writing – review & editing, Supervision. **Jordi Pallarès:** Writing – review & editing, Supervision, Resources, Project administration, Funding acquisition, Conceptualization. **Jure Ravnik:** Writing – review & editing, Supervision, Resources, Project administration, Funding acquisition, Conceptualization.

Declaration of competing interest

The authors declare that they have no known competing financial interests or personal relationships that could have appeared to influence the work reported in this paper.

Acknowledgments

The authors thank the Deutsche Forschungsgemeinschaft for the financial support in the framework of the project STE 544/75-1 and the Slovenian Research and Innovation Agency (research core funding No. P2-0196 and project J7-60118). NC, SC, SV and JP acknowledge the funding of the Ministerio de Ciencia, Innovación y Universidades under project PID2023-146648NB-C21 and the support of the Departament de Recerca i Universitats de la Generalitat de Catalunya (2021SGR00732).

Appendix A. Relevance of forces

To assess the relative significance of the various force terms in the Maxey–Riley–Gatignol equation, we express Eq. (4) in non-dimensional form. This is done using the characteristic length and velocity scales of the problem, denoted by L_0 and u_0, respectively (Cui et al., 2018). Introducing the dimensionless variables $\boldsymbol{v}^* = \boldsymbol{v}/u_0$, $\boldsymbol{u}^* = \boldsymbol{u}/u_0$, and $t^* = tu_0/L_0$, the equation becomes

$$\frac{d\boldsymbol{v}^*}{dt^*} = \frac{A}{\mathrm{Stk}}\left[\boldsymbol{v}_s^* + \frac{a_3}{3d_{\mathrm{eq}}}\boldsymbol{K}\cdot\left[\boldsymbol{u}^* - \boldsymbol{v}^*\right]\right] + \frac{3}{2}R\frac{\partial \boldsymbol{u}^*}{\partial t^*} + R\left[\left[\boldsymbol{u}^* + \frac{1}{2}\boldsymbol{v}^*\right]\cdot\boldsymbol{\nabla}\right]\boldsymbol{u}^* \tag{A.1}$$

Moreover, we can separate the spherical and non-spherical contributions to the drag and write:

$$\frac{d\boldsymbol{v}^*}{dt^*} = \frac{A}{\mathrm{Stk}}\left[\boldsymbol{v}_s^* + \left[\boldsymbol{u}^* - \boldsymbol{v}^*\right] + \left[\frac{c}{3d_{\mathrm{eq}}}\boldsymbol{K} - \boldsymbol{I}\right]\cdot\left[\boldsymbol{u}^* - \boldsymbol{v}^*\right]\right] + \frac{3}{2}R\frac{\partial \boldsymbol{u}^*}{\partial t^*} + R\left[\left[\boldsymbol{u}^* + \frac{1}{2}\boldsymbol{v}^*\right]\cdot\boldsymbol{\nabla}\right]\boldsymbol{u}^* \tag{A.2}$$

where $\boldsymbol{I}$ denotes the identity tensor. Using the non-dimensional Eq. (A.1)–(A.2), it can be seen that the importance of gravity and drag force scale with the factor A/Stk, while the pressure gradient and added mass term scale with the factor R, Cui et al. (2018). In this context, the nondimensional parameters A and R depend on the fluid–particle ratio and are obtained as follows (Cui et al., 2018)

$$R = \frac{\rho_{\mathrm{f}}}{\rho_{\mathrm{p}} + 0.5\rho_{\mathrm{f}}}, \quad A = \frac{\rho_{\mathrm{p}}}{\rho_{\mathrm{p}} + 0.5\rho_{\mathrm{f}}}. \tag{A.3}$$

In addition, Stk denotes the Stokes number, which describes the ratio of the characteristic particle response time τ_{p} to a characteristic time of the flow τ_{f}. The Stokes number of a particle with volume-equivalent sphere diameter d_{eq} is obtained as follows

$$\mathrm{Stk} = \frac{\tau_\mathrm{p}}{\tau_\mathrm{f}} = \frac{\rho_\mathrm{p}}{\rho_\mathrm{f}} \frac{d_\mathrm{eq}^2 u_0}{18 \nu_\mathrm{f} L_0} . \tag{A.4}$$

The characteristic time scales of the particle τ_p and the flow τ_f are obtained as follows

$$\tau_\mathrm{p} = \frac{\rho_\mathrm{p}}{\rho_\mathrm{f}} \frac{d_\mathrm{eq}^2}{18 \nu_\mathrm{f}} , \quad \tau_\mathrm{f} = \frac{L_0}{u_0} . \tag{A.5}$$

Note that the pressure gradient and added mass force can be considered negligible compared to the reduced gravity and drag force if $\rho_\mathrm{p} \gg \rho_\mathrm{f}$ and thus $R \ll 1$, see Eq. (A.3), Cui et al. (2018). However, even if $\rho_\mathrm{p} \approx \rho_\mathrm{f}$, the impact of the additional forces can be considered minor compared to $\boldsymbol{f}_\mathrm{GB}$ and $\boldsymbol{f}_\mathrm{D}$ if the Stokes number is sufficiently small ($\mathrm{Stk} \ll 1$) and consequently $A/\mathrm{Stk} \gg 1$, see Eq. (A.3)–(A.4).

The terminal velocity of a particle is reached when the sum of the flow-induced frictional and the buoyant forces on the particle balances the gravitational force $\boldsymbol{f}_\mathrm{D}$. In case of a spherical particle settling in Stokes flow, the terminal velocity $\boldsymbol{v}_\mathrm{s}$ is given by: (Crowe, 2000)

$$\boldsymbol{v}_\mathrm{s} = \frac{d_\mathrm{eq}^2}{18 \nu_\mathrm{f}} \frac{\rho_\mathrm{p} - \rho_\mathrm{f}}{\rho_\mathrm{f}} \boldsymbol{g} . \tag{A.6}$$

Appendix B. Tensor coefficients for prolate spheroidal ellipsoids

Followingly, the coefficients of $\underline{K}'$ can be written as

$$K'_{22} = K'_{33} = \frac{16 \left[\lambda^2 - 1\right]^{3/2}}{\left[2\lambda^2 - 3\right] \ln(\lambda + \sqrt{\lambda^2 - 1}) + \lambda \sqrt{\lambda^2 - 1}} , \tag{B.1}$$

$$K'_{11} = \frac{8 \left[\lambda^2 - 1\right]^{3/2}}{\left[2\lambda^2 - 1\right] \ln(\lambda + \sqrt{\lambda^2 - 1}) - \lambda \sqrt{\lambda^2 - 1}} , \tag{B.2}$$

In the limit of a spherical particle shape, the resistance tensor is given by

$$\lim_{\lambda \to 1} \underline{K}' = 6 \, \underline{I} , \tag{B.3}$$

where $\underline{I}$ denotes the identity matrix, leading to $K_{11} = K_{22} = K_{33} = 6$.

The moment of inertia tensor components of a general ellipsoidal particle (prolate, oblate, triaxial) with half-axis a_1, a_2, and a_3 ($a_1 \geq a_2 \geq a_3$) in the pFoR expands as (Jaklič and Solina, 2003)

$$J_{11} = \frac{4}{15} \pi \rho a_1 a_2 a_3 \left[a_2^2 + a_3^2\right] \tag{B.4}$$

$$J_{22} = \frac{4}{15} \pi \rho a_1 a_2 a_3 \left[a_1^2 + a_3^2\right] \tag{B.5}$$

$$J_{33} = \frac{4}{15} \pi \rho a_1 a_2 a_3 \left[a_1^2 + a_2^2\right] \tag{B.6}$$

For prolate ellipsoidal particles ($\lambda_1 = \lambda$, $\lambda_2 = 1$) $\underline{\Pi}'$ and $\underline{\Omega}'$ read as

$$\underline{\Pi}' = \frac{16 \, \lambda}{3} \left[1 - \lambda^2\right] \begin{bmatrix} 0 \\ \left[\beta_0 + \lambda^2 \, \gamma_0\right]^{-1} \\ -\left[\alpha_0 + \lambda^2 \, \gamma_0\right]^{-1} \end{bmatrix} \quad \text{and}$$

$$\underline{\Omega}' = \frac{16 \, \lambda}{3} \begin{bmatrix} 2\left[\alpha_0 + \beta_0\right]^{-1} \\ \left[\beta_0 + \lambda^2 \, \gamma_0\right]^{-1} \left[1 + \lambda^2\right] \\ \left[\alpha_0 + \lambda^2 \, \gamma_0\right]^{-1} \left[1 + \lambda^2\right] \end{bmatrix} \tag{B.7}$$

by using the non-dimensional coefficients α_0, β_0 and γ_0, which expand as follows (Gallily and Cohen, 1979),

$$\alpha_0 = \beta_0 = \frac{\lambda^2}{\lambda^2 - 1} + \frac{\lambda}{2[\lambda^2 - 1]^{3/2}} \ln \left[\frac{\lambda - \sqrt{\lambda^2 - 1}}{\lambda + \sqrt{\lambda^2 - 1}}\right] , \tag{B.8}$$

$$\gamma_0 = -\frac{2}{\lambda^2 - 1} - \frac{\lambda}{[\lambda^2 - 1]^{3/2}} \ln \left[\frac{\lambda - \sqrt{\lambda^2 - 1}}{\lambda + \sqrt{\lambda^2 - 1}}\right] . \tag{B.9}$$

In the limit of spherical particle shape ($\lambda_1 = \lambda_2 = 1$) the nondimensional coefficients render $\alpha_0 = \beta_0 = \lambda\gamma_0 = 2/3$, leading to:

- $\Omega'_{11} = \Omega'_{22} = \Omega'_{33} = 8$ and
- $\Pi'_{11} = \Pi'_{22} = \Pi'_{33} = 0$

Appendix C. Particle deposition model

As discussed by Feng and Kleinstreuer (2013), non-spherical particles, such as ellipsoids and fibers, exhibit more complex deposition behavior than spherical particles. For spherical particles, wall contact is assumed to occur when the Euclidean distance between the particle centroid $\boldsymbol{r}_c$ and the nearest point on the wall $\boldsymbol{r}_w$ is less than or equal to the particle radius, i.e., $\|\boldsymbol{r}_c - \boldsymbol{r}_w\|_2 \leq d/2$.

For adhesive (sticky) walls, such as mucus-coated airways, particle deposition is assumed to occur immediately upon contact between the particle and the wall (Feng and Kleinstreuer, 2013). Note that determining deposition for non-spherical particles is more involved than for spheres, as three distinct contact scenarios must be considered (Feng and Kleinstreuer, 2013):

I. if $\|\boldsymbol{r}_c - \boldsymbol{r}_w\|_2 \leq a_3 \rightarrow$ particle will deposit.
II. if $\|\boldsymbol{r}_c - \boldsymbol{r}_w\|_2 > a_1 \rightarrow$ particle does not touch the wall.
III. if $a_3 < \|\boldsymbol{r}_c - \boldsymbol{r}_w\|_2 \leq a_1 \rightarrow$ particle deposits depending on its orientation.

Here, a_3 denotes the smallest semi-axis, and a the semi-major axis of the ellipsoidal particle under consideration. In the following, we focus on the deposition algorithm corresponding to the third case, i.e., $a_3 < \|\boldsymbol{r}_c - \boldsymbol{r}_w\|_2 \leq a_1$. In this context, the equation of the wall is introduced. Let $\hat{\boldsymbol{h}}$, $\hat{\boldsymbol{j}}$, and $\hat{\boldsymbol{k}}$ denote three non-collinear points lying on a planar wall, defined in a reference frame with its origin located on the wall. The corresponding wall normal vector expands then as follows:

$$\boldsymbol{n} = \frac{\left[\hat{\boldsymbol{k}} - \hat{\boldsymbol{h}}\right] \times \left[\hat{\boldsymbol{j}} - \hat{\boldsymbol{h}}\right]}{\left|\left[\hat{\boldsymbol{k}} - \hat{\boldsymbol{h}}\right] \times \left[\hat{\boldsymbol{j}} - \hat{\boldsymbol{h}}\right]\right|} , \tag{C.1}$$

leading to the wall equation:

$$W = \boldsymbol{n} \cdot \left[\boldsymbol{r} - \hat{\boldsymbol{h}}\right] = 0 , \tag{C.2}$$

with an arbitrary wall point $\boldsymbol{r} = [x, y, z]'$. Furthermore, the ellipsoidal particle surface is defined as follows:

$$E(r') = \left[\frac{x'}{a_1}\right]^2 + \left[\frac{y'}{a_2}\right]^2 + \left[\frac{z'}{a_3}\right]^2 , \tag{C.3}$$

which is written in the particle frame of reference (pFoR). Any position $r' = [x', y', z']$ with $E(r') \leq 1$ belongs to the ellipsoid with $E(r') = 1$ describing the particle surface. The parameters a_1, a_2, a_3 in Eq. (C.3) denote the particle half-axis with $a_1 \geq a_2 \geq a_3$.

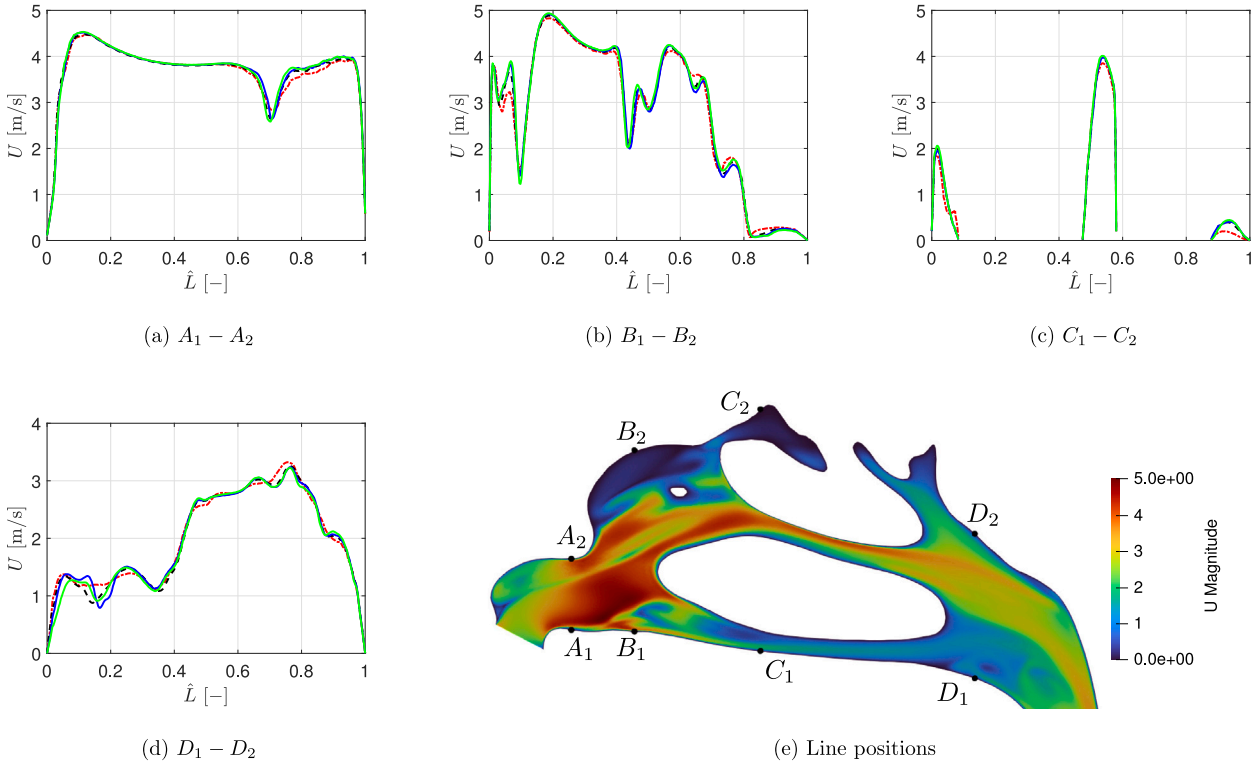
Note that, within the context of the present work, an established particle–wall contact is assumed to result in particle deposition. A brief sketch of the algorithm used to detect particle–wall contact is provided in the following:

Algorithm 1: Wall deposition model

```
forall particles do
    forall wall faces in interaction distance do
        if ||r_c − r_w||_2 ≤ a_3: contact to wall
        if ||r_c − r_w||_2 > a_1: no contact to wall
        if a_3 < ||r_c − r_w||_2 ≤ a_1:
            map wall data to positive octant of ellipsoid surface E
            find r by solving optimization problem: min(E(r, r_c, ϵ))
        with the constraint W(r, n, ĥ) = 0
            if E(r, r_c, ϵ) ≤ 1 → particle–wall contact (→ particle
        deposits).
    end
end
```

Appendix D. Mesh study: velocity and turbulent kinetic energy profiles

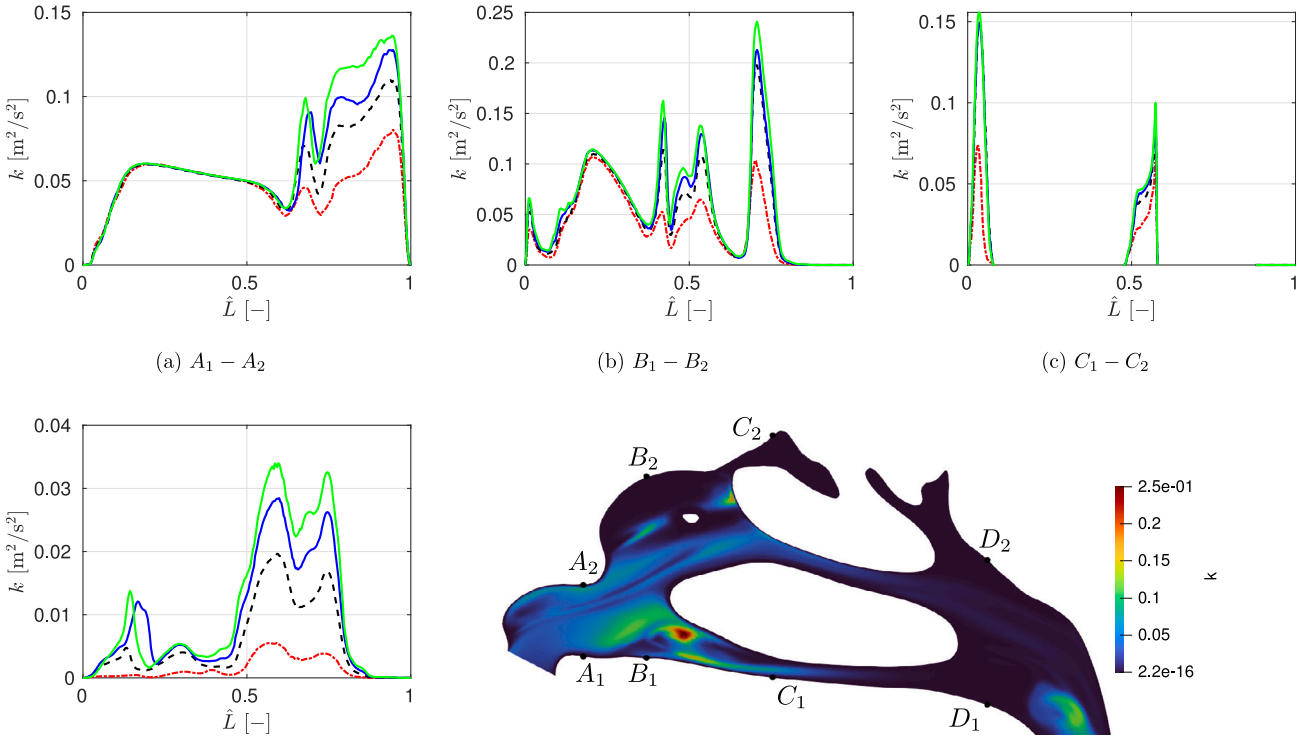
To enable a more quantitative comparison between the meshes, velocity and turbulent kinetic energy k profiles are presented next along four selected lines traversing the nasal airways.



(a) $A_1 - A_2$ (b) $B_1 - B_2$ (c) $C_1 - C_2$

(d) $D_1 - D_2$ (e) Line positions

Fig. D.22. Velocity magnitude U profile along four selected lines. Displayed results: M0, M1, M2, M3. In addition, the velocity magnitude distribution is visualized in the L1 plane.



(a) $A_1 - A_2$ (b) $B_1 - B_2$ (c) $C_1 - C_2$

(d) $D_1 - D_2$ (e) Line positions

Fig. D.23. Turbulent kinetic energy k profile along four selected lines. Displayed results: M0, M1, M2, M3. In addition, the velocity magnitude distribution is visualized in the L1 plane.

As displayed in Fig. D.22, a clear convergence of velocity profiles is observed across all selected lines with increasing mesh resolution. The line positions are highlighted in Fig. D.22(e). This convergence indicates that $M1$ provides sufficient resolution to accurately capture the velocity distribution within the nasal airways.

In addition to the velocity profiles, the turbulent kinetic energy k profiles across all selected lines also converge with increasing mesh resolution, as illustrated in Fig. D.23 (line positions indicated in Fig. D.23(e)). The deviations between $M2$ and $M3$ are significantly smaller than those between $M0$ and $M1$. Considering the balance between accuracy and computational efficiency, $M2$ is selected for further analysis, as it sufficiently resolves both the velocity and turbulent kinetic energy within the nasal airways.

Data availability

Data will be made available on request.

References

Abolhassantash, M., Tavakol, M., Abouali, O., Yaghoubi, M., Ahmadi, G., 2020. Deposition fraction of ellipsoidal fibers in the human nasal cavity- influence of non-creeping formulation of hydrodynamic forces and torques. Int. J. Multiph. Flow 126, 103238. http://dx.doi.org/10.1016/j.ijmultiphaseflow.2020.103238.

Balachandar, S., Soldati, A., 2020. Editorial: Multiphase flow community must have a role in predicting host-to-host airborne contagion. Int. J. Multiph. Flow 132, 103440. http://dx.doi.org/10.1016/j.ijmultiphaseflow.2020.103440.

Balachandar, S., Zaleski, S., Soldati, A., Ahmadi, G., Bourouiba, L., 2020. Host-to-host airborne transmission as a multiphase flow problem for science-based social distance guidelines. MedRxiv http://dx.doi.org/10.1101/2020.08.28.20183814.

Brenner, H., 1963. The Stokes resistance of an arbitrary particle. Chem. Eng. Sci. 18, 1–25.

Brüning, J., Hildebrandt, T., Heppt, W., Schmidt, N., Lamecker, H., Szengel, A., Amiridze, N., Ramm, H., Bindernagel, M., Zachow, S., et al., 2020. Characterization of the airflow within an average geometry of the healthy human nasal cavity. Sci. Rep. 10 (1), 3755.

Bui, V.K.H., Moon, J.-Y., Chae, M., Duck-Shin, P., Young-Chul, L., 2020. Prediction of aerosol deposition in the human respiratory tract via computational models: A review with recent updates. Atmosphere 137.

Corda, J.V., Shenoy, B.S., Ahmad, K.A., Lewis, L., K, P., Rao, A., Zuber, M., 2024. Comparison of microparticle transport and deposition in nasal cavity of three different age groups. Inhal. Toxicol. 36 (1), 44–56. http://dx.doi.org/10.1080/08958378.2024.2312801.

Crowe, C., 2000. On models for turbulence modulation in fluid-particle flows. Int. J. Multiph. Flow 26 (5), 719–727.

Cui, Y., Ravnik, J., Hriberšek, M., Steinmann, P., 2018. On constitutive models for the momentum transfer to particles in fluid-dominated two-phase flows. Adv. Struct. Mater. 80, 1–25.

Dang Khoa, N., Phuong, N.L., Takahashi, K., Ito, K., 2022. Transport and deposition of inhaled man-made vitreous and asbestos fibers in realistic human respiratory tract models: An in silico study. Jpn. Archit. Rev. 5 (4), 592–608.

Dastan, A., Abouali, O., Ahmadi, G., 2014. CFD simulation of total and regional fiber deposition in human nasal cavities. J. Aerosol Sci. 69, 132–149.

Dong, J., Sun, Q., Shang, Y., Zhang, Y., Tian, L., Tu, J., 2022. Numerical comparison of inspiratory airflow patterns in human nasal cavities with distinct age differences. Int. J. Numer. Methods Biomed. Eng. 38 (3), e3565.

Fan, F.-G., Ahmadi, G., 1995. A sublayer model for wall deposition of ellipsoidal particles in turbulent streams. J. Aerosol Sci. 26 (5), 813–840. http://dx.doi.org/10.1016/0021-8502(95)00021-4.

Farkas, Á., Balásházy, I., 2008. Quantification of particle deposition in asymmetrical tracheobronchial model geometry. Comput. Biol. Med. 38, 508–518. http://dx.doi.org/10.1016/j.compbiomed.2008.01.014.

Farkas, Á., Lizal, F., Elcner, J., Jedelsky, J., Jicha, M., 2019. Numerical simulation of fibre deposition in oral and large bronchial airways in comparison with experiments. J. Aerosol Sci. 136, 1–14. http://dx.doi.org/10.1016/j.jaerosci.2019.06.003.

Feng, Y., Kleinstreuer, C., 2013. Analysis of non-spherical particle transport in complex internal shear flows. Phys. Fluids 25, 091904. http://dx.doi.org/10.1063/1.4821812.

Ferziger, J.H., Perić, M., 2008. Numerische strömungsmechanik. Springer, Berlin Heidelberg.

Gallily, I., Cohen, A.-H., 1979. On the orderly nature of the motion of nonspherical aerosol particles II. Inertial collision between a spherical large droplet and axially symmetrical elongated particle. J. Colloid Interface Sci. 68, 338–356.

Ganser, G.H., 1993. A rational approach to drag prediction of spherical and nonspherical particles. Powder Technol. 77 (2), 143–152. http://dx.doi.org/10.1016/0032-5910(93)80051-B.

Garcia, G.J.M., Tewksbury, E.W., Wong, B.A., Kimbell, J.S., 2009. Interindividual variability in nasal filtration as a function of nasal cavity geometry. J. Aerosol Med. 22, 139–155.

Gatignol, R., 1983. The faxén formulae for a rigid particle in an unsteady non-uniform Stokes-flow. J. Mćanique Thórique AppliquÉ 1, 143–160.

Goldstein, H., 1980. Classical Mechanics, second ed. Addison Wesley, Reading, MA, USA.

Gorlé, C.v., Van Beeck, J., Rambaud, P., Van Tendeloo, G., 2009. CFD modelling of small particle dispersion: the influence of the turbulence kinetic energy in the atmospheric boundary layer. Atmos. Environ. 43 (3), 673–681.

Greifzu, F., Kratzsch, C., Forgber, T., Lindner, F., Schwarze, R., 2016. Assessment of particle-tracking models for dispersed particle-laden flows implemented in OpenFOAM and ANSYS FLUENT. Eng. Appl. Comput. FluidMechanics 10 (1), 30–43.

Gualtieri, A.F., 2023. Journey to the centre of the lung. The perspective of a mineralogist on the carcinogenic effects of mineral fibres in the lungs. J. Hazard. Mater. 442, 130077.

Guilmette, R.A., Cheng, Y.S., Griffith, W.C., 1997. Characterising the variability in adult human nasal airway dimensions. Ann. Occup. Hyg. 41 (Suppl. 1), 491–496.

Haider, A., Levenspiel, O., 1989. Drag coefficient and terminal velocity of spherical and nonspherical particles. Powder Technol. 58 (1), 63–70.

Hartman, M., Trnka, O., Svoboda, K., Veselý, V., 1994. Influence of particle shape on the drag coefficient for isometric particles. Collect. Czechoslov. Chem. Commun. 59 (12), 2583–2594.

Hinds, W.C., 1999. Aerosol Technology: Properties, Behavior, and Measurement of Airborne Particles. Wiley-Interscience, New York.

Holmér, I., Kuklane, K., Gao, C., 2007. Minute volumes and inspiratory flow rates during exhaustive treadmill walking using respirators. Ann. Occup. Hyg. 51 (3), 327–335. http://dx.doi.org/10.1093/annhyg/mem004.

Hsu, D.-J., Chuang, M.-H., 2012. In-vivo measurements of micrometer-sized particle deposition in the nasal cavities of Taiwanese adults. Aerosol Sci. Technol. 46 (6), 631–638. http://dx.doi.org/10.1080/02786826.2011.652749.

Hu, Z., Ma, R., Wang, Y., Lou, M., Gong, M., Wang, B., Zheng, G., Dong, J., Zhang, Y., 2023. Quantitative study of artemisia pollens deposition in the upper airways of children with adenoidal hypertrophy. J. Aerosol Sci. 172, 106191.

Int Panis, L., de Geus, B., Vandenbulcke, G., Willems, H., Degraeuwe, B., Bleux, N., Mishra, V., Thomas, I., Meeusen, R., 2010. Exposure to particulate matter in traffic: A comparison of cyclists and car passengers. Atmos. Environ. 44 (19), 2263–2270. http://dx.doi.org/10.1016/j.atmosenv.2010.04.028.

Inthavong, K., Shang, Y., Del Gaudio, J.M., Wise, S.K., Edwards, T.S., Bradshaw, K., Wong, E., Smith, M., Singh, N., 2021. Inhalation and deposition of spherical and pollen particles after middle turbinate resection in a human nasal cavity. Respir. Physiol. Neurobiol. 294, 103769. http://dx.doi.org/10.1016/j.resp.2021.103769.

Inthavong, K., Tian, Z., Tu, J., Yang, W., Xue, C., 2008. Optimising nasal spray parameters for efficient drug delivery using computational fluid dynamics. Comput. Biol. Med. 38 (6), 713–726. http://dx.doi.org/10.1016/j.compbiomed.2008.03.008.

Inthavong, K., Zhang, K., Tu, J., 2011. Numerical modelling of nanoparticle deposition in the nasal cavity and the tracheobronchial airway. Comput. Methods Biomech. Biomed. Eng. 14 (7), 633–643. http://dx.doi.org/10.1080/10255842.2010.493510.

Jaklič, A., Solina, F., 2003. Moments of superellipsoids and their application to range image registration. IEEE Trans. Syst. Man Cybern. Part B Cybern. : A Publ. IEEE Syst. Man Cybernetics Soc. 33, 648–657. http://dx.doi.org/10.1109/TSMCB.2003.814299.

Jia, L., Zhang, L., Yu, S., 2018. Deposition of non-spherical microparticles in the human upper respiratory tract. Particuology 36, 185–189. http://dx.doi.org/10.1016/j.partic.2017.06.009.

Jundi, X., 2016. Modification of stochastic model in Lagrangian tracking method. In: Nilsson, H. (Ed.), CFD with OpenSource Software.

Kelly, J.T., Asgharian, B., Kimbell, J.S., Wong, B.A., 2004a. Particle deposition in human nasal airway replicas manufactured by different methods. Part I: Inertial regime particles. Aerosol Sci. Technol. 38 (11), 1063–1071. http://dx.doi.org/10.1080/027868290883360.

Kelly, J.T., Asgharian, B., Kimbell, J.S., Wong, B.A., 2004b. Particle deposition in human nasal airway replicas manufactured by different methods. Part II: Ultrafine particles. Aerosol Sci. Technol. 38 (11), 1072–1079. http://dx.doi.org/10.1080/027868290883432.

Kleinstreuer, C., Feng, Y., 2013. Computational analysis of non-spherical particle transport and deposition in shear flow with application to lung aerosol dynamics—A review. J. Biomech. Eng. 135, 021008. http://dx.doi.org/10.1115/1.4023236.

Koelmans, A.A., Redondo-Hasselerharm, P.E., Nor, N.H.M., de Ruijter, V.N., Mintenig, S.M., Kooi, M., 2022. Risk assessment of microplastic particles. Nat. Rev. Mater. 7 (2), 138–152.

Koullapis, P.G., Kassinos, S.C., Muela, J., Perez-segarra, C., Rigola, J., Lehmkuhl, O., Cui, Y., Sommerfeld, M., Elcner, J., Jicha, M., Saveljic, I., Filipovic, N., Lizal, F., Nicolaou, L., 2017. Regional aerosol deposition in the human airways : The SimInhale benchmark case and a critical assessment of in silico methods. Eur. J. Pharm. Sci. 113, 1–18. http://dx.doi.org/10.1016/j.ejps.2017.09.003.

Lancmanová, A., Bodnar, T., 2025. Numerical simulations of human respiratory flows: a review. Discov. Appl. Sci. 7, http://dx.doi.org/10.1007/s42452-025-06617-x.
Li, Z., Kleinstreuer, C., Zhang, Z., 2007. Particle deposition in the human tracheobronchial airways due to transient inspiratory flow patterns. J. Aerosol Sci. 38, 625–644. http://dx.doi.org/10.1016/j.jaerosci.2007.03.010.
Liu, Y., Cao, Y., Li, H., Liu, H., Bi, L., Chen, Q., Peng, R., 2024. A systematic review of microplastics emissions in kitchens: Understanding the links with diseases in daily life. Environ. Int. 108740.
Liu, Y., Johnson, M.R., Matida, E.A., Kherani, S., Marsan, J., 2009. Creation of a standardized geometry of the human nasal cavity. J. Appl. Physiol. 106, 784–795.
Liu, Y., Matida, E.A., Gu, J., Johnson, M.R., 2007. Numerical simulation of aerosol deposition in a 3-D human nasal cavity using RANS, RANS/EIM, and LES. J. Aerosol Sci. 38 (7), 683–700. http://dx.doi.org/10.1016/j.jaerosci.2007.05.003.
Maxey, M.R., Riley, J.J., 1983. Equation of motion for a small rigid sphere in a nonuniform flow. Phys. Fluids 26 (4), 883–889. http://dx.doi.org/10.1063/1.864230.
Menter, F.R., 1994. Two-equation eddy-viscosity turbulence models for engineering applications. AIAA J. 32, 1598–1605.
Nihart, A.J., Garcia, M.A., El Hayek, E., Liu, R., Olewine, M., Kingston, J.D., Castillo, E.F., Gullapalli, R.R., Howard, T., Bleske, B., et al., 2025. Bioaccumulation of microplastics in decedent human brains. Nature Med. 1–6.
OpenFOAM The OpenFOAM Foundation, 2025. OpenFOAM Foundation repository for OpenFOAM version 11.
Paplińska-Goryca, M., Misiukiewicz-Stepień, P., Wróbel, M., Mycroft-Rzeszotarska, K., Adamska, D., Rachowka, J., Królikowska, M., Goryca, K., Krenke, R., 2025. The impaired response of nasal epithelial cells to microplastic stimulation in asthma and COPD. Sci. Rep. 15 (1), 4242.
Prata, J.C., 2018. Airborne microplastics: Consequences to human health? Environ. Pollut. 234, 115–126. http://dx.doi.org/10.1016/j.envpol.2017.11.043.
Prinz, F., Kánská, J., Elcner, J., Hájek, O., Kummerländer, A., Krause, M., Jícha, M., Lizal, F., 2025. Transport and deposition of inhaled fibers in a realistic female airway model: A combined experimental and numerical study. Comput. Biol. Med. 194, 110473. http://dx.doi.org/10.1016/j.compbiomed.2025.110473.
Rahim, W.A., Faizal, W.M., Ghazali, N.N.N., Khor, C.Y., Badruddin, I., Zainon, M., Yazid, A., Ibrahim, N., Razi, R., 2020. Computational fluid dynamics modelling of human upper airway: A review. Comput. Methods Programs Biomed. 196, 105627. http://dx.doi.org/10.1016/j.cmpb.2020.105627.
Ravnik, J., Štrakl, M., Wedel, J., Steinmann, P., Hriberšek, M., 2022. Stokes Flow Induced Drag and Torque on Asbestos-Like Fibres Cannot Be Estimated by a Simplistic Ellipsoidal Approximation. WIT Press, pp. 33–44.
Riaz, H.H., Lodhi, A.H., Munir, A., Zhao, M., Ali, M.H., Sauret, E., Gu, Y., Islam, M.S., 2025. Breath of pollutants: How breathing patterns influence microplastic accumulation in the human lung. Int. J. Multiph. Flow 185, 105156. http://dx.doi.org/10.1016/j.ijmultiphaseflow.2025.105156.
Rostami, A., 2009. Computational modeling of aerosol deposition in respiratory tract: A review. Inhal. Toxicol. 21, 262–290. http://dx.doi.org/10.1080/08958370802448987.
Schroeter, J.D., Garcia, G.J., Kimbell, J.S., 2011. Effects of surface smoothness on inertial particle deposition in human nasal models. J. Aerosol Sci. 42 (1), 52–63. http://dx.doi.org/10.1016/j.jaerosci.2010.11.002.
Shachar-Berman, L., Bhardwaj, S., Ostrovski, Y., Das, P., Koullapis, P., Kassinos, S., Sznitman, J., 2020. In silico optimization of fiber-shaped aerosols in inhalation therapy for augmented targeting and deposition across the respiratory tract. Pharmaceutics 12 (3), 230. http://dx.doi.org/10.3390/pharmaceutics12030230.
Shang, Y., Inthavong, K., Tu, J., 2015. Detailed micro-particle deposition patterns in the human nasal cavity influenced by the breathing zone. Comput. & Fluids 114, 141–150. http://dx.doi.org/10.1016/j.compfluid.2015.02.020.
Shen, Z., Tolu Mekonne, T., Cai, X., Milton-McGurk, L., Chan, H.-K., Kourmatzis, A., Cheng, S., 2025. Experimental measurements of particle deposition in the human nasal airway. Int. J. Pharm. 672, 125280. http://dx.doi.org/10.1016/j.ijpharm.2025.125280.
Shi, H., Kleinstreuer, C., Zhang, Z., 2007. Modeling of inertial particle transport and deposition in human nasal cavities with wall roughness. J. Aerosol Sci. 38 (4), 398–419. http://dx.doi.org/10.1016/j.jaerosci.2007.02.002.
Singh, M., Briones, M., O'Hagan, D.T., 2001. A novel bioadhesive intranasal delivery system for inactivated influenza vaccines. J. Control. Release 70 (3), 267–276. http://dx.doi.org/10.1016/S0168-3659(00)00330-8.
Stöber, W., 1972. Dynamic shape factors of nonspherical aerosol particles. In: Assessment of Airborne Particles. pp. 249–289.
Štrakl, M., Hriberšek, M., Wedel, J., Steinmann, P., Ravnik, J., 2022. A model for translation and rotation resistance tensors for superellipsoidal particles in Stokes flow. J. Mar. Sci. Eng. 10 (3), 369.
Strelets, M., 2001. Detached eddy simulation of massively separated flows. http://dx.doi.org/10.2514/6.2001-879.
Tadas, P., Dainius, M., Edvinas, K., Linas, K., Maksim, K., Axel, Z., 2011. Comparative characterization of particle emissions from asbestos and non-asbestos cement roof slates. Build. Environ. 46 (11), 2295–2302.
Tang, Y., Guo, B., 2011. Computational fluid dynamics simulation of aerosol transport and deposition. Front. Environ. Sci. Eng. China 5, 362–377. http://dx.doi.org/10.1007/s11783-011-0365-8.
Tran-Cong, S., Gay, M., Michaelides, E.E., 2004. Drag coefficients of irregularly shaped particles. Powder Technol. 139 (1), 21–32. http://dx.doi.org/10.1016/j.powtec.2003.10.002.
Tretiakow, D., Tesch, K., Markiet, K., Przewoźny, T., Kusiak, A., Cichońska, D., Skorek, A., 2023. Numerical analysis of the ostiomeatal complex aeration using the CFD method. Sci. Rep. 13 (1), 3980.
Tretiakow, D., Tesch, K., Markiet, K., Skorek, A., 2022. Maxillary sinus aeration analysis using computational fluid dynamics. Sci. Rep. 12 (1), 10376.
Vianello, A., Jensen, R.L., Liu, L., Vollertsen, J., 2019. Simulating human exposure to indoor airborne microplastics using a breathing thermal manikin. Sci. Rep. 9, 8670. http://dx.doi.org/10.1038/s41598-019-45054-w.
Wadell, H., 1933. Sphericity and roundness of rock particles. J. Geol. 41 (3), 310–331. http://dx.doi.org/10.1086/624040.
Wang, J., Alipour, M., Soligo, G., Roccon, A., Paoli, M.D., Picano, F., Soldati, A., 2021. Short-range exposure to airborne virus transmission and current guidelines. Proc. Natl. Acad. Sci. 118 (37), e2105279118. http://dx.doi.org/10.1073/pnas.2105279118.
Wang, S., Inthavong, K., Wen, J., Tu, J., Xue, C., 2009. Comparison of micron-and nanoparticle deposition patterns in a realistic human nasal cavity. Respir. Physiol. Neurobiol. 166 (3), 142–151.
Wedel, J., Steinmann, P., Štrakl, M., Hriberšek, M., Cui, Y., Ravnik, J., 2022. Anatomy matters: The role of the subject-specific respiratory tract on aerosol deposition - A CFD study. Comput. Methods Appl. Mech. Engrg. 401, 115372.
Wedel, J., Steinmann, P., Štrakl, M., Hriberšek, M., Ravnik, J., 2021a. Risk Assessment of Infection by Airborne Droplets and Aerosols at Different Levels of Cardiovascular Activity. Arch. Comput. Methods Eng. 28 (6), 4297–4316. http://dx.doi.org/10.1007/s11831-021-09613-7.
Wedel, J., Steinmann, P., Štrakl, M., Hriberšek, M., Ravnik, J., 2023. Shape matters: Lagrangian tracking of complex nonspherical microparticles in superellipsoidal approximation. Int. J. Multiph. Flow 158, 104283. http://dx.doi.org/10.1016/j.ijmultiphaseflow.2022.104283.
Wedel, J., Štrakl, M., Hriberšek, M., Steinmann, P., Ravnik, J., 2024. A novel particle–particle and particle–wall collision model for superellipsoidal particles. Comput. Part. Mech. 11, 211–234. http://dx.doi.org/10.1007/s40571-023-00618-6.
Wedel, J., Štrakl, M., Steinmann, P., Hriberšek, M., Ravnik, J., 2021b. Can CFD establish a connection to a milder COVID-19 disease in younger people? Comput. Mech. 67, 1497–1513. http://dx.doi.org/10.1007/s00466-021-01988-5.
Weinberger, S.E., Cockrill, B.A., Mandel, J., 2014. 1 - pulmonary anatomy and physiology: The basics. In: Weinberger, S.E., Cockrill, B.A., Mandel, J. (Eds.), Principles of Pulmonary Medicine (Sixth Edition), Sixth ed. W.B. Saunders, Philadelphia, pp. 1–19. http://dx.doi.org/10.1016/B978-1-4557-2532-8.00001-3.
Weller, H.G., Tabor, G., Jasak, H., Fureby, C., 1998. A tensorial approach to computational continuum mechanics using object orientated techniques. Comput. Phys. 12, 620–631. http://dx.doi.org/10.1063/1.168744.
White, F.M., 2008. Fluid Mechanics. McGraw-Hill Companies, Inc., New York.
World Health Organization; International Labour Organization, 2021. WHO/ILO Joint Estimates of the Work-Related Burden of Disease and Injury, 2000–2016: global Monitoring Report. Tech. Rep., World Health Organization, Geneva.
Yang, Z., Wang, M., Feng, Z., Wang, Z., Lv, M., Chang, J., Chen, L., Wang, C., 2023. Human microplastics exposure and potential health risks to target organs by different routes: A review. Curr. Pollut. Rep. 9 (3), 468–485.
Zamankhan, P., Ahmadi, G., Wang, Z., Hopke, P.K., Cheng, Y.-S., Su, W.C., Leonard, D., 2006. Airflow and deposition of nano-particles in a human nasal cavity. Aerosol Sci. Technol. 40 (6), 463–476.
Zarus, G.M., Muianga, C., Hunter, C.M., Pappas, R.S., 2021. A review of data for quantifying human exposures to micro and nanoplastics and potential health risks. Sci. Total Environ. 756, 144010.
Zhang, L., Asgharian, B., Anjilvel, S., 1996. Inertial and interceptional deposition of fibers in a bifurcating airway. J. Aerosol Med. 9 (3).
Zhang, Y., Kang, S., Allen, S., Allen, D., Gao, T., Sillanpää, M., 2020. Atmospheric microplastics: A review on current status and perspectives. Earth-Sci. Rev. 203, 103118.
Zhang, Z., Kleinstreuer, C., 2011. Laminar-to-turbulent fluid–nanoparticle dynamics simulations: Model comparisons and nanoparticle-deposition applications. Int. J. Numer. Methods Biomed. Eng. 27, 1930–1950.
Zhang, M., Liu, T., Zhang, L., Hua, Z., Guo, Z., Dong, J., Tan, Q., Xie, Y., Yin, X., Yan, L., et al., 2024. Assessment of microplastic exposure in nasal lavage fluid and the influence of face masks. J. Hazard. Mater. 480, 136069.